HHS Public Access

Author manuscript

Cell Rep. Author manuscript; available in PMC 2021 November 22.

Published in final edited form as:

Cell Rep. 2021 November 02; 37(5): 109917. doi:10.1016/j.celrep.2021.109917.

Temporal dynamics of base excision/single-strand break repair protein complex assembly/disassembly are modulated by the PARP/NAD+/SIRT6 axis

Christopher A. Koczor[1,2], **Kate M. Saville**[1,2], **Joel F. Andrews**[1], **Jennifer Clark**[1,2], **Qingming Fang**[1,2], **Jianfeng Li**[1,2], **Rasha Q. Al-Rahahleh**[1,2], **Md Ibrahim**[1,2], **Steven McClellan**[1], **Mikhail V. Makarov**[1,2], **Marie E. Migaud**[1,2], **Robert W. Sobol**[1,2,3,*]

[1]Mitchell Cancer Institute, University of South Alabama, Mobile, AL 36604, USA

[2]Department of Pharmacology, College of Medicine, University of South Alabama, Mobile, AL 36604, USA

[3]Lead contact

SUMMARY

Assembly and disassembly of DNA repair protein complexes at DNA damage sites are essential for maintaining genomic integrity. Investigating factors coordinating assembly of the base excision repair (BER) proteins DNA polymerase β (Polβ) and XRCC1 to DNA lesion sites identifies a role for Polβ in regulating XRCC1 disassembly from DNA repair complexes and, conversely, demonstrates Polβ's dependence on XRCC1 for complex assembly. LivePAR, a genetically encoded probe for live-cell imaging of poly(ADP-ribose) (PAR), reveals that Polβ and XRCC1 require PAR for repair-complex assembly, with PARP1 and PARP2 playing unique roles in complex dynamics. Further, BER complex assembly is modulated by attenuation/augmentation of NAD^+ biosynthesis. Finally, SIRT6 does not modulate PARP1 or PARP2 activation but does regulate XRCC1 recruitment, leading to diminished Polβ abundance at sites of DNA damage. These findings highlight coordinated yet independent roles for PARP1, PARP2, and SIRT6 and their regulation by NAD^+ bioavailability to facilitate BER.

Graphical abstract

*Correspondence: rwsobol@southalabama.edu.

AUTHOR CONTRIBUTIONS

C.A.K., K.M.S., and R.W.S. designed the experiments. C.A.K., K.M.S., J.F.A., J.C., Q.F., J.L., R.Q.A.-R., M.I., and S.M. conducted the experiments. J.F.A. developed software (MIDAS). M.V.M. and M.E.M. synthesized and provided critical reagents. C.A.K. and R.W.S wrote the paper. All authors read, commented on, and approved the final manuscript version.

SUPPLEMENTAL INFORMATION

Supplemental information can be found online at https://doi.org/10.1016/j.celrep.2021.109917.

DECLARATION OF INTERESTS

R.W.S. is a scientific consultant for Canal House Biosciences, but this company was not involved in this study, nor was the consulting work related to this study. The authors declare no competing interests.

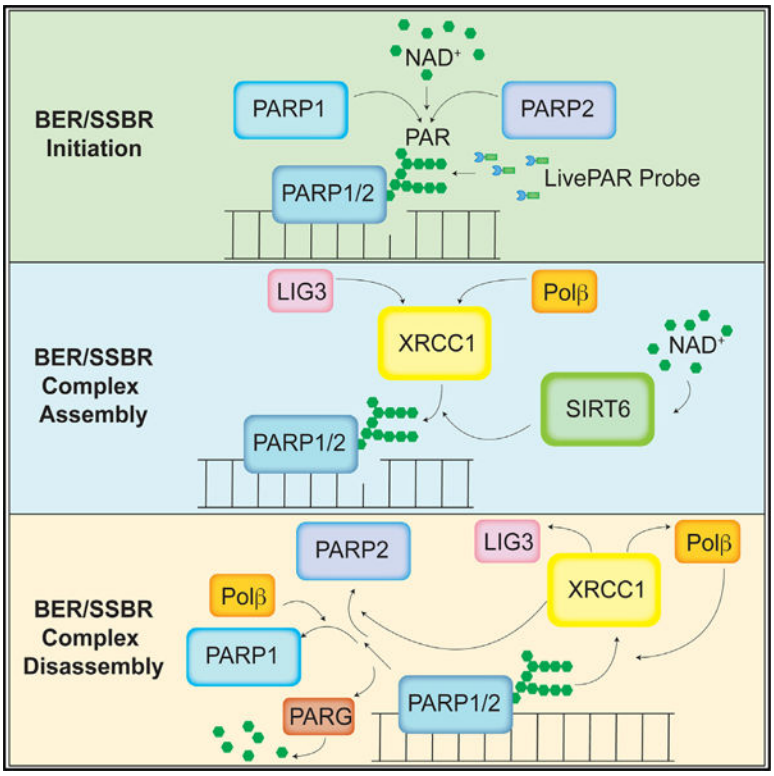

In brief

Koczor et al. use quantitative confocal microscopy to characterize DNA-damage-induced poly(ADP-ribose) (PAR) formation and assembly/disassembly kinetics in human cells. These studies highlight the coordinated yet independent roles for XRCC1, POLB, PARP1, PARP2, and SIRT6 (and regulation by NAD^+) to facilitate BER/SSBR protein complex dynamics.

INTRODUCTION

DNA repair pathways rely on the coordinated expression, synthesis, and post-translational modification (PTM) of multiple proteins and the bioavailability of regulatory factors to repair DNA lesions, including (1) signaling to promote chromatin access and DNA repair-complex assembly, (2) localization of repair complex scaffold proteins, (3) activity of enzymatic repair proteins, (4) disassembly of the repair complex, and (5) chromatin reorganization.

Base excision repair (BER) and single-strand break repair (SSBR) mechanisms facilitate repair of base damage and DNA single-strand breaks (SSBs) (Abbotts and Wilson, 2017; Svilar et al., 2011) (Figure 1A). Short-patch BER begins with removal of the damaged base by a DNA glycosylase, followed by apurinic/apyrimidinic (AP) site processing by AP-endonuclease 1 (APE1) and gap tailoring by the 5′-deoxyribosephosphate (dRP) lyase function of DNA polymerase β (Polβ). The nucleotidyl-transferase activity of Polβ then inserts a new base, followed by DNA ligase 1 (LIG1) or DNA ligase 3 (LIG3)-mediated ligation to seal the phosphodiester backbone (Sobol et al., 2000; Wilson and Barsky,

2001). Efficient recruitment of BER/SSBR proteins to sites of damage relies on key protein-protein interactions and PTMs. X-ray repair cross-complementing 1 (XRCC1) functions as a scaffold protein that localizes repair proteins (including Polβ and LIG3) to DNA damage sites (Almeida and Sobol, 2007; London, 2015). XRCC1 is recruited through its poly(ADP-ribose) (PAR)-binding domain, which binds to PAR chains, a PTM formed by activated PAR polymerases (PARPs) at sites of DNA damage (Breslin et al., 2015; El-Khamisy et al., 2003). Loss of one or more of these assembly intermediates or proteins would be expected to compromise BER/SSBR complex formation by reducing Polβ localization to sites of DNA damage. This appears to be the case for NAD^+-dependent protein deacetylase sirtuin 6 (SIRT6). Loss of SIRT6 increased genomic instability and enhanced sensitivity to DNA damage (Mostoslavsky et al., 2006).

Another factor critical to genome stability is the co-factor nicotinamide adenine dinucleotide (NAD^+) (Fouquerel and Sobol, 2014; Saville et al., 2020). NAD^+ is an essential substrate for PARPs (such as PARP1) and sirtuins (such as SIRT6), allowing each to perform a number of genome-stabilizing activities (Imai and Guarente, 2014; Rouleau et al., 2010). A deficiency in NAD^+ can lead to decreased PARP and sirtuin activity, increased genomic instability, and decreased DNA repair capacity (Fouquerel et al., 2014). NAD^+ levels have been shown to decrease with aging (Fang et al., 2017; Imai and Guarente, 2014), during pregnancy (Shi et al., 2017), and upon viral infection (Mesquita et al., 2016) and are dysregulated in some cancers (Chiarugi et al., 2012; Yaku et al., 2018). Augmenting NAD^+ through pharmacological means has been of increasing interest (Giroud-Gerbetant et al., 2019; Montllor-Albalate et al., 2021). Dihydronicotinamide riboside (NRH) is a reduced form of nicotinamide riboside (NR) and is uniquely metabolized, rapidly leading to enhanced levels of intracellular NAD^+ (Giroud-Gerbetant et al., 2019; Yang et al., 2019). The extent that cellular NAD^+ pools can be modulated in cancer cells, and how this impacts the assembly and disassembly of BER/SSBR complexes at sites of DNA damage is currently unknown.

While the *in vitro* biochemistry of the proteins in the BER and SSBR pathways have been extensively studied, the mechanisms by which key repair proteins assemble and disassemble at the DNA damage site in the cell are not fully defined. Biochemical analysis of DNA lesions processed by BER proteins using purified nucleosomes suggests additional factors are likely required to effectively gain access to the DNA lesion for removal and repair (Beard et al., 2003; Cole et al., 2010; Rodriguez et al., 2017). Laser micro-irradiation provides real-time assessment of DNA repair in live cells within the cellular context of other factors known to alter DNA repair, including chromatin structure, non-enzymatic accessory proteins, and the cellular metabolic profile. Here, real-time *in vivo* assembly and disassembly of BER/SSBR complexes were investigated using UVA laser micro-irradiation to introduce lesions repaired primarily via BER/SSBR (Holton et al., 2017). To follow PARP activation in real time, we developed a genetically encoded PAR monitor (LivePAR), demonstrating enhanced capacity to characterize BER/SSBR by real-time analysis of PAR formation in cells. Further, we show that BER/SSBR complex assembly is modulated by alterations in NAD^+ bioavailability. Finally, we highlight that, unlike its role in DNA double-strand break (DSB) repair (DSBR) (Tian et al., 2019), SIRT6 does not regulate PAR synthesis during BER yet negatively impacts XRCC1's complex assembly capacity (independent of PAR formation) and ultimately reduces Polβ's localization to sites of DNA

damage. Overall, these studies highlight the coordinated yet independent roles for PARP1, PARP2, and SIRT6 and their regulation by NAD^+ to facilitate BER, supporting an essential PARP/NAD^+/SIRT6 axis for BER protein-complex assembly dynamics.

RESULTS

Dynamics of Polβ and XRCC1 BER complex assembly

To quantitatively assess the recruitment of DNA repair proteins in response to laser-induced micro-irradiation, we used MIDAS (Modular Irradiation, Detection, and Analysis System), a complete software platform for performing and analyzing micro-irradiation experiments (see STAR Methods). We first established recruitment kinetics for the central protein factors in BER, Polβ, and XRCC1 (Figure 1A). While 405-nm laser micro-irradiation introduces both DNA SSBs and DNA DSBs, 355-nm lasers preferentially produce BER- and SSBR-specific damage when used at appropriate laser powers (Holton et al., 2017; Lan et al., 2004). We observed recruitment of the fluorescently tagged DNA DSBR protein 53BP1 to sites of 405-nm micro-irradiation, but not to sites of 355-nm micro-irradiation, demonstrating that the 355-nm laser does not produce a measurable DSB response in our experimental system (Figures S1A and S1B). Additionally, 24 h pre-treatment with 10 μM bromodeoxyuridine (BrdU) can be used to sensitize cells to UVA-induced DNA damage (Rosenstein et al., 1980). 53BP1 recruited to sites of 355-nm-induced DNA damage following BrdU sensitization, although with lower intensity than the 405-nm laser alone (Figures S1A and S1B). Thus, using 355-nm stimulation without BrdU sensitization allows investigation of the response of Polβ and XRCC1 to BER/SSBR selective DNA damage in the absence of significant DNA DSBR and response from DSBR proteins.

Fluorescently tagged Polβ and XRCC1 rapidly recruited to 355-nm laser-induced DNA damage in U2OS cells (Figures 1B, 1C, and S1C; Tables S3 and S4). Although Polβ and XRCC1 are considered to form a heterodimer during DNA repair (Almeida and Sobol, 2007), Polβ was found to reach maximum recruitment capacity more rapidly (time to peak intensity, ~30 s) than XRCC1 (time to peak intensity, ~90 s). Recruitment kinetics were different for both proteins in A549 cells as compared to U2OS cells, demonstrating the importance of cell-type-specific context for repair-complex assembly and disassembly (Figures S2A–S2D). Similar peak recruitment times (time to peak) between Polβ and XRCC1 were observed (A549 cells), though the half-life of recruitment was prolonged for XRCC1. When A549 cells were sensitized by treatment with the photosensitizer BrdU (10 μM), both the time to peak and half-life of recruitment for Polβ were significantly faster compared to untreated cells (Figures S2A and S2B). XRCC1 recruitment kinetics did not change significantly following BrdU sensitization, though peak intensity was increased in BrdU-treated cells (Figures S2C and S2D). These results support a model whereby Polβ and XRCC1 may have independent regulation of recruitment kinetics to sites of DNA damage.

LivePAR enables real-time, live-cell PAR imaging

To overcome limitations of immunocytochemistry for PAR analysis, we developed a fluorescently tagged PAR-binding fusion protein, LivePAR, a live-cell imaging probe for poly(ADP-ribose) (PAR) (Figure 1D). Ten PAR-binding domains (PBDs) from known PAR-

binding proteins were identified (Table S1) (Teloni and Altmeyer, 2016). Each PBD was fused to EGFP, expressed in cells, and imaged to ensure expression. We visualized the response of each fusion protein to 355-nm laser-induced DNA damage under similar micro-irradiation conditions employed for Polβ and XRCC1 recruitment. Among the ten fusion proteins, only the WWE domain from RNF146 (when fused to EGFP; hereafter termed LivePAR) demonstrated recruitment to sites of 355-nm micro-irradiation during our initial screen (Figures 1E, 1F, and S1C). Mutations that eliminate binding of the LivePAR PBD (WWE domain of RNF146) to PAR have been characterized (Wang et al., 2012). Expression of LivePAR harboring the Y107A mutation was sufficient to prevent LivePAR recruitment to micro-irradiation induced sites of DNA damage (Figure 1F). PARP inhibition (ABT-888, veliparib) prevented LivePAR's recruitment to laser-induced foci, while Poly(ADP-ribose) glycohydrolase (PARG) inhibition (PDD00017273) enhanced and prolonged LivePAR's recruitment (Figure 1G). LivePAR therefore is a stable, live-cell imaging tool for visualizing PAR formation and degradation in real-time in living cells. Combining LivePAR with laser micro-irradiation yields a powerful experimental platform for probing the mechanistic processes affecting DNA repair-complex assembly (Figure 1A).

The macrodomain from H2A1.1 (Timinszky et al., 2009) and the BRCT1 domain from XRCC1 (Breslin et al., 2015) may also be used to track PAR formation following micro-irradiation in cells. In our initial screen, neither domain displayed foci following 355-nm laser micro-irradiation, so we investigated these PBDs further. The BRCT1 domain from XRCC1 is attributed to amino acids 315–405 (London, 2015; UniProt Consortium, 2021); however, the BRCT1 domain used for micro-irradiation experiments in Breslin et al. consisted of amino acids 161–405, which includes the XL1 linker region (Breslin et al., 2015). We added the XL1/BRCT1(161–405) domain to our screen to investigate the role of this XL1 linker region on recruitment kinetics. To enhance our screen, we (1) increased the length of 355-nm laser micro-irradiation from 1 s to 2.5 s, (2) utilized BrdU to photosensitize cells (Rosenstein et al., 1980), and (3) included 405-nm laser micro-irradiation with and without BrdU photosensitization. Upon increasing the laser duration from 1 s to 2.5 s, we visualized LivePAR recruitment, but only faint recruitment of both the BRCT1 and the macrodomain were observed (Figure S2E). Under these conditions, the LivePAR probe was 13 times more sensitive than the macrodomain and 7 times more sensitive than XRCC1's BRCT1 domain at detecting micro-irradiation induced PAR. Recruitment of the XL1/BRCT1 domain was stronger than either the BRCT1 or the macrodomain but had a more prolonged recruitment profile compared to LivePAR, BRCT1, or the macrodomain (Figure S2E). Recruitment of the BRCT1 domain and the macrodomain was more readily observed following BrdU sensitization, but signal detection was saturated for LivePAR recruitment; this limited intensity comparisons but facilitated better recruitment kinetic comparisons (Figure S2F). Recruitment kinetics for LivePAR, the BRCT1 domain, and the macrodomain (H2A1.1) were all similar (time to peak ~65–75 s), while the half-life of recruitment varied for each (range of ~180–280 s), with no statistically significant difference (Figure S2G). While the XL1/BRCT domain demonstrated stronger recruitment intensity, it displayed a significantly longer time to peak intensity (~250 s) and half-life of recruitment (~440 s) as compared to the other three PBDs; this suggests that while the XL1/BRCT domain may recruit in a PAR-dependent manner, the addition of XL1

alters recruitment kinetics of the BRCT1 domain alone (Figures S2E and S2F). Finally, we re-examined the remaining PBDs from our initial screen; none produced focal recruitment following prolonged 355-nm laser micro-irradiation, 405-nm laser micro-irradiation, or BrdU sensitization at either wavelength. These results do not suggest that the PBDs or the proteins from which they are derived cannot bind PAR; rather, the PBDs chosen were taken out of the context of their respective proteins, and the additional protein structures may enhance PAR-binding characteristics. This is readily observed here in the difference between the recruitment of the BRCT1 domain, the XL1/BRCT1 domain, and XRCC1 itself; each produce different recruitment kinetics and intensities, but the BRCT1 domain itself is the site of PAR binding. Additional considerations (such as the length of the linker between the PBD and EGFP and the use of a C-terminal EGFP as opposed to an N-terminal EGFP) may also impact PAR-binding capacity of these domains. These results document that the LivePAR probe is more sensitive for PAR detection than previously published PBD fusions while demonstrating similar recruitment kinetics to known PBDs.

We further validated the LivePAR probe by comparison to PAR immunofluorescence. A549/LivePAR cells demonstrated focal recruitment following micro-irradiation, and fixed cells showed similar co-localization when stained with a PAR antibody (Figure S3A). Due to the lower nuclear background observed in PAR-antibody-labeled samples, the initial relative fluorescence intensity was higher in PAR immunofluorescent samples as compared to LivePAR, which had a higher background level. The signal of both LivePAR and PAR immunofluorescence decreased with time (Figure S3B), consistent with previous results (Figure 1F) and in agreement with the conclusion that LivePAR is detecting PAR levels in real time. Finally, we compared the intensity of PAR immunofluorescence in A549 cells to that found in A549/LivePAR cells. The LivePAR-expressing cells (A549/LivePAR) showed lower PAR immunofluorescence intensity, suggesting that the LivePAR probe and the PAR antibody are competing for binding to PAR (Figure S3C).

We then used the parallel laser micro-irradiation module in MIDAS to quantitatively assess and compare recruitment dynamics for the key BER factors Polβ, XRCC1, and PAR (LivePAR), measuring the time to peak recruitment intensity and half-life of recruitment (Figures 1H and 1I). Polβ reached peak recruitment intensity first, followed by XRCC1 and then LivePAR. Similarly, analysis of the half-life of recruitment demonstrated that Polβ disassembles from the repair complex first, followed by XRCC1 and then the degradation of PAR, as evidenced by the long half-life of LivePAR in U2OS cells. To validate the time to recruitment observed by parallel micro-irradiation, we performed serial micro-irradiation. Unlike parallel micro-irradiation, where ten cells are micro-irradiated and then time corrected for simultaneous imaging at 15-s imaging intervals, serial micro-irradiation analyzes one cell and images at an interval of 250 ms for a duration of 1 min. Using equivalent laser micro-irradiation as in the parallel analysis, serial analysis confirmed the 30-s time to peak intensity for Polβ following the 355-nm stimulation in U2OS cells and validated the accuracy of the parallel analysis module while reducing the observed error (Figures 1J–1L).

Overexpression of EGFP-Polβ displays similar recruitment kinetics as endogenously tagged EGFP-Polβ

To address if overexpression of the fluorescently tagged DNA repair proteins altered recruitment kinetics, EGFP cDNA was fused endogenously to the POLB gene in A549 cells, thereby preserving the promoter region and allowing expression of the EGFP-Polβ protein under endogenous cellular and genomic conditions (Figure 2A; Table S5). Successful generation of cells expressing EGFP-Polβ was confirmed through three independent methods. Sanger sequencing of POLB alleles demonstrated successful targeting of one of the three alleles in A549 cells (Figure 2B; Table S2); one allele was modified with the EGFP open reading frame inserted in-frame at the 5′ end of exon 1 (Figure 2B), one allele had no modification, and the final allele had a partial incorporation that added 45 base pairs 5′ to POLB exon 1. Immunoblots showed that both EGFP-Polβ and non-tagged Polβ were produced by the modified A549 cells (Figure 2C; full blots in Figure S4A). Finally, we performed confocal spectral microscopy to confirm that EGFP-Polβ was detected in the modified A549 cells. Because expression under the endogenous POLB promoter led to low levels of EGFP fluorescence in the modified cells, we performed spectral imaging and unmixing to remove autofluorescence. Spectral unmixing demonstrated that EGFP-Polβ expression was primarily in the nuclear compartment, with a minor fraction in the cytosolic compartment, consistent with the distribution observed in EGFP-Polβ-overexpressing cells (Figures 2D and S4B). Endogenously expressed EGFP-Polβ recruited to sites of 355-nm laser-induced DNA damage and recruitment kinetics were similar to cells with overexpressed EGFP-Polβ (Figures 2D–2G). The half-life of recruitment for the endogenously tagged EGFP-Polβ was significantly reduced as compared to overexpressed EGFP-Polβ in A549 cells (Figure 2G). This may be a result of the increased amount of Polβ protein that can recruit to the site of damage in overexpression models, resulting in a slight increase in the time required to disassemble the Polβ complex. Therefore, we find that overexpression of EGFP-Polβ does not lead to gross changes in recruitment kinetics when compared to EGFP-Polβ expressed at endogenous levels.

Loss of Polβ enzymatic activity does not alter damage-induced recruitment kinetics

Polβ has two enzymatic functions: (1) a 5′dRP lyase activity that can be significantly attenuated by an alanine mutation at amino acid residue K72 (K72A) and (2) a polymerase or nucleotidyl-transferase activity that can be eliminated by an alanine mutation at residue D256 (D256A) (Matsumoto et al., 1998; Menge et al., 1995). Loss of the 5′dRP lyase activity of Polβ, but not its polymerase activity, sensitizes cells to genotoxic damage, suggesting that loss of the 5′dRP lyase activity may enhance retention of Polβ to sites of DNA damage (Sobol et al., 2000). Surprisingly, no significant changes in recruitment kinetic profiles, time to peak intensity, or half-life of recruitment were observed when comparing EGFP-Polβ, EGFP-Polβ(K72A), and EGFP-Polβ(D256A) expressed in U2OS cells (Figures 3A–3C and S5A). As residual endogenous Polβ could contribute to the repair of laser-induced DNA damage, the wild-type (WT) and mutant fusions were modified to be gRNA resistant and then expressed in U2OS/POLB-KO cells (Figures 3D and S5A). However, loss of endogenous Polβ had no effect on the recruitment profiles of either the dRP lyase or polymerase mutants (Figure 3E). Polβ(K72A) has 1% residual 5′dRP lyase activity (Sobol et al., 2000), but the EGFP-Polβ 5′dRP lyase triple mutant Polβ(K35A/K68A/K72A) is

completely devoid of 5′dRP lyase activity (Sobol et al., 2000) and also was unaltered as compared to EGFP-Polβ in POLB-knockout cells (U2OS/POLB-KO) (Figures 3F and S5B). To identify if this was a U2OS-cell-specific outcome, A549/POLB-KO cells were used to verify the 5′dRP lyase activity mutant results. Again, no change in recruitment was observed in the EGFP-Polβ(K72A)-expressing cells as compared to EGFP-Polβ (Figures S5C–S5E). In all, we find that EGFP-Polβ recruitment to and retention at sites of DNA damage is not dependent on either of Polβ's known enzymatic functions.

Polβ is known to bind to chromatin through XRCC1-dependent and independent mechanisms (Fang et al., 2019), and it is possible that Polβ mutants may exhibit altered chromatin binding and nuclear mobility that may confound interpretation of recruitment kinetics. To determine if Polβ mobility to sites of DNA damage is altered upon mutation, we performed fluorescence recovery after photobleaching (FRAP) experiments. Using U2OS/POLB-KO cells to reduce the contribution of endogenous Polβ, we found that cells expressing EGFP-Polβ(K72A), EGFP-Polβ(K35A/K68A/K72A), and EGFP-Polβ(D256A) all displayed similar nuclear mobility to EGFP-Polβ following photobleaching, suggesting that none of the amino acid changes altered the mobility of Polβ within the nucleus (Figure S5G and S5H).

Polβ's recruitment is dependent on XRCC1, while Polβ enables XRCC1 complex disassociation

Recruitment to and retention of Polβ at micro-irradiation-induced DNA damage sites may be regulated through one of its binding partners. A candidate for this role is XRCC1, which functions as a scaffold for multiple repair proteins, including Polβ, at sites of DNA damage (Kubota et al., 1996). Loss of XRCC1 (Figures 4A and S6A) attenuated Polβ recruitment to sites of DNA damage (Figure 4B). Pre-treatment with a PARG inhibitor was not able to rescue Polβ recruitment in XRCC1-KO cells (Figure 4B). Because XRCC1-KO can promote genomic instability, which could cause or contribute to the observed reduction in Polβ recruitment, we investigated genomic stability and cell growth in the XRCC1-KO cell lines (Ensminger et al., 2014; Lee et al., 2009). The doubling times of U2OS/Cas9, U2OS/POLB-KO(1.7), and U2OS/XRCC1-KO(E2) cell lines were similar (~31 h), while U2OS/XRCC1-KO(E3) cells demonstrated slower growth (doubling time, ~56 h) (Figure S6B). There was no difference in cell-cycle phase distribution between any of the cells, suggesting no specific cell-cycle checkpoint was being initiated in U2OS/XRCC1-KO(E3) cells (Figure S6C). Immunofluorescence revealed an increase in γH2AX foci in U2OS/XRCC1-KO(E3) cells, consistent with some genomic instability in that cell line, but this was not observed in U2OS/XRCC1-KO(E2) cells (Figure S6D). Finally, we re-expressed XRCC1 in the corresponding XRCC1-KO cell lines, which rescued Polβ recruitment and facilitated Polβ foci formation in both XRCC1-KO cell lines (Figures S6E and S6F). This suggests that XRCC1 is required for BER complex assembly for Polβ, but it does not address if physical binding between the two proteins is required. A separation-of-function mutation in the V303 loop of Polβ (L301R/V303R/V306R), referred to as Polβ(TM), reduces the binding affinity between Polβ and XRCC1 greater than 6-fold (Fang et al., 2014, 2019). EGFP-Polβ(TM) was expressed in A549 cells expressing endogenous XRCC1 and did not visibly recruit

to sites of laser micro-irradiation (Figures 4C and S7A), demonstrating that the physical interaction between Polβ and XRCC1 is required to facilitate Polβ recruitment.

We next investigated if alterations (loss) in Polβ expression could modulate XRCC1 recruitment. XRCC1-EGFP recruitment exhibited both enhanced peak recruitment intensity and prolonged recruitment in POLB-KO cells when compared to Pol-β-expressing cells (Figure 4D). This suggests that Polβ is required to facilitate XRCC1 dissociation from assembled DNA repair complexes. To validate this, Polβ and XRCC1-EGFP were co-expressed in POLB-KO cells. By re-expressing Polβ, we were able to recapitulate XRCC1's disassociation from micro-irradiation-induced foci, thereby demonstrating a requirement for Polβ to promote rapid dissociation of XRCC1 from the site of DNA damage (Figures 4E and S7B). Re-expressing Polβ with either the dRP lyase triple mutant (K35A/K68A/K72A) or the polymerase mutant (D256A) also led to normalization of XRCC1 recruitment kinetics, suggesting that the enzymatic activity of Polβ is not facilitating XRCC1 dissociation (Figures 4I and 4J). These results suggest a negative feedback loop in which Polβ requires XRCC1 for recruitment to sites of DNA damage but then itself acts as a regulator of XRCC1 dissociation from those sites via heterodimer (XRCC1/Polβ) complex formation.

The dependence on Polβ for XRCC1 dissociation may be mediated by enhanced PARylation at the site of DNA damage in the absence of Polβ, as Polβ loss would likely lead to prolonged PAR formation at the site of damage (Jelezcova et al., 2010; Tang et al., 2010). We then utilized the LivePAR probe to interrogate PAR dynamics in POLB-KO cells. PARylation was enhanced in POLB-KO cells compared to normal cells, but the rate of PAR degradation was similar in POLB-KO cells compared to Polβ-expressing cells (Figure 4F). Re-expressing Polβ rescued this phenotype and reduced LivePAR recruitment intensity (Figures S7F and S7G). We demonstrated that the retention of XRCC1 at sites of DNA damage is dependent on PAR formation in POLB-KO cells by adding PARP inhibitor (ABT-888) after laser-induced foci had formed (~200 s following stimulation; Figure S7E). This suggests that loss of Polβ enhances the retention of XRCC1 through a PARP-mediated PARylation mechanism.

We investigated this increased PARylation by expressing PARP1-EGFP and PARP2-EGFP fusion proteins in WT, POLB-KO, and XRCC1-KO U2OS cells. PARP1 showed prolonged recruitment kinetics in both POLB-KO and XRCC1-KO cells (Figures S8A and S8B). PARP2 recruitment was unchanged in POLB-KO cells as compared to U2OS WT cells; however, PARP2 showed prolonged recruitment in XRCC1-KO cells, suggesting that PARP2's recruitment was affected by a POLB-independent, XRCC1-mediated process (Figures S8C and S8D). Our data support a model whereby enhanced PARylation in POLB-KO cells is mediated by prolonged PARP1 retention at sites of DNA damage, likely promoting increased PARylation and XRCC1 retention. As the retention of XRCC1 could be rescued by enzymatically inactive Polβ mutants (Figures S7C and S7D), this would suggest that Polβ mediates the dissociation of XRCC1 through a function not related to its known enzymatic functions. Finally, we confirmed that the BER protein LIG3 did not recruit in XRCC1-KO cells or following PARP inhibition (Figure 4G). Interestingly, LIG3 recruitment was unchanged in POLB-KO cells when compared to WT cells, suggesting that during

prolonged XRCC1 recruitment in POLB-KO cells, LIG3 dissociates from DNA damage foci independent of Polβ expression.

Polβ and XRCC1 complex dynamics depend on PAR formation and degradation

Polβ recruitment was attenuated, but not eliminated, in PARP1-KO cells (Figure 5A), consistent with findings that other PARPs (such as PARP2) promote PARylation and DNA repair-complex assembly during BER (Figure 5B) (Dantzer et al., 2000; Schreiber et al., 2002). Loss of PARP2 slightly attenuated Polβ recruitment, but loss of both PARP1 and PARP2 eliminated Polβ recruitment (Figures 5C and S9A). PARylation, as determined by the recruitment of the LivePAR probe, was abolished with PARP inhibition (ABT-888), while PARG inhibition (PDD00017273) enhanced and prolonged PAR formation (Figure 1G). Polβ and XRCC1 behaved similarly, showing attenuation of recruitment upon PARP inhibition and prolonged recruitment/retention following PARG inhibition (Figures 5D and 5E). However, knockout of TARG (OARD1), which removes the O-acyl-ADP-ribose moiety on the target protein (Sharifi et al., 2013), did not alter Polβ recruitment kinetics (Figures S9B and S9C). Polβ recruitment was not rescued in PARG-inhibitor-treated XRCC1-KO cells, suggesting that enhanced Polβ recruitment in PARG inhibited cells is mediated through Polβ's interaction with XRCC1 (Figure 4B). PAR synthesis/degradation therefore temporally regulates Polβ and XRCC1 repair-complex assembly and disassembly at DNA damage sites.

Polβ and XRCC1 complex assembly is regulated by NAD^+ availability

To identify how NAD^+ availability affects Polβ/XRCC1 repair complex formation, the NAMPT inhibitor FK866 was used to decrease cellular NAD^+ levels, and NRH was used to enhance cellular NAD^+ levels (Giroud-Gerbetant et al., 2019; Yang et al., 2019). Although NRH is stable in fetal bovine serum (FBS), there are several factors in FBS that may alter the stability of other NAD^+ catabolites (Giroud-Gerbetant et al., 2019; Wilk et al., 2020), so we used heat-inactivated FBS (HI-FBS). We noted that the recruitment profiles of Polβ, XRCC1, and LivePAR in HI-FBS were similar to cells cultured in FBS (Figures S10A–S10C).

FK866 diminished NAD^+ levels in U2OS cells to 23% (Figure 6A). Since the conversion of NRH to NAD^+ is dependent on the metabolic profile of the cell (Giroud-Gerbetant et al., 2019; Yang et al., 2019), we identified when NAD^+ levels were maximally enhanced following NRH administration (Figure 6B). Peak NAD^+ levels were observed 4 h post-NRH addition (~850% increase), with NAD^+ levels above controls for up to 8 h. NRH also enhanced DNA-damage-(H_2O_2)-induced PARylation in U2OS cells, an effect attenuated by FK866 or ABT-888 treatment (Figure 6C). In laser micro-irradiation experiments, NRH enhanced peak recruitment intensities of Polβ (45%), XRCC1 (94%), and LivePAR (88%) (Figures 6D–6F). Conversely, FK866 reduced peak recruitment intensities of Polβ (37%), XRCC1 (35%), and LivePAR (24%) (Figure 6G–6I). Overall, NAD^+ availability does not impact repair-complex assembly or disassembly other than to increase or decrease the magnitude of recruitment.

LN428 cells also exhibited increased NAD^+ levels and enhanced PARP1 activation following NRH supplementation (Figures S10D and S10E). Interestingly, NRH did not significantly increase NAD^+ in A549 cells (Figure 6B), possibly due to the low expression of adenosine kinase (The Human Protein Atlas, 2020; Uhlen et al., 2017; Yang et al., 2020) or enhanced NADH/NRH conversion (e.g., via NUDIX5), among other mechanisms of NRH metabolism/catabolism (Sonavane et al., 2020). We found no change in NADH following NRH supplementation in either A549 or U2OS cells (Figure S10F). U2OS and A549 cell lines provided a unique opportunity to identify effects (if any) of NRH on DNA repair-complex assembly independent of its NAD^+-enhancing capability. Following NRH treatment, A549 cells did not show enhanced Polβ, XRCC1, or LivePAR recruitment kinetics but remained sensitive to FK866 (Figures S11A–S11F). We find that NRH's enhancement of NAD^+ therefore directly impacts damage-induced PAR synthesis and the recruitment of Polβ, XRCC1, and LivePAR to sites of DNA damage.

Loss of SIRT6 impairs Polβ and XRCC1 complex assembly without altering PAR formation

SIRT6 was previously documented to play a critical role in BER-mediated repair, but the exact mechanism has never been resolved (Mostoslavsky et al., 2006). It was suggested that SIRT6 may modulate repair by regulating PARP1 (Mao et al., 2011) and that SIRT6 is required for PARP1 activation in DSB repair (Tian et al., 2019). We evaluated the role of SIRT6 on Polβ and XRCC1 recruitment and PAR formation in response to DNA damage (Figure 7A). There was no change in cellular NAD^+ levels in SIRT6-KO cells, suggesting loss of SIRT6 would not indirectly alter PARylation (Figure S12A). In the absence of SIRT6, both Polβ and XRCC1 demonstrated significantly diminished recruitment to DNA damage (Figures 7B and 7C). However, PAR formation was not altered in SIRT6-KO cells (Figure 7D). When compared to A549/Cas9 cells, A549/SIRT6-KO cells demonstrated no overall effect on PAR immunofluorescence (by two-way ANOVA) or in individual comparisons to A549/Cas9 cells at individual time points (by Bonferroni) (Figures S12E and S12F). Given that SIRT6 can impact chromatin remodeling, we investigated if loss of SIRT6 alters Polβ recruitment due to decreased mobility to sites of DNA damage. However, using FRAP analysis, we found that EGFP-Polβ mobility was unchanged in SIRT6-KO cells as compared to WT cells (Figures 7E and 7F).

We then determined if re-expression of SIRT6 could rescue the deficiency of Polβ recruitment in SIRT6-KO cells. SIRT6 is known to have at least two enzymatic functions, mono-ADP-ribosylation activity and deacetylation activity (Mao et al., 2012). We investigated if the co-expression of EGFP-Polβ with either WT SIRT6 or the SIRT6 separation-of-function mutants could be used to determine which of SIRT6's known enzymatic functions regulate Polβ recruitment. Expressing either the deacetylation deficient SIRT6(R65A) mutant or the mono-ADP-ribosylation deficient SIRT6(G60A) mutant was able to restore Polβ recruitment, while expressing SIRT6(S56Y), which has been shown to be catalytically dead, also was able to rescue Polβ recruitment (Figure S12B–S12D). These results suggest that SIRT6 regulates the recruitment of Polβ via a currently unknown enzymatic function or through some structural interaction not related to its deacetylation or mono-ADP-ribosylation activities. Together, these results support a model where SIRT6

enhances XRCC1's binding to PAR at sites of DNA damage and loss of SIRT6 diminishes XRCC1 (and by extension Polβ) recruitment to sites of DNA damage (Figure 7G).

DISCUSSION

The characterization of DNA repair-complex assembly and disassembly remains an intense area of investigation for multiple biological fields, including cellular DNA damage response, somatic hypermutation, class-switch recombination, gene regulation, stem cell differentiation, cancer, and aging. Identification of substrates, enzymes, and accessory factors that are part of and that regulate such complexes are key in refining our models of DNA repair pathway control and crosstalk. While the sequence of enzymatic steps required to repair BER/SSBR lesions has been biochemically characterized using *in vitro* assays, laser micro-irradiation of fluorescently tagged repair proteins enables interrogation of the repair process within an intact cellular context, allowing analysis of the effects of loss or modulation of key DNA repair or other cellular components. Therefore, we took advantage of the added throughput and flexibility of the MIDAS software system to perform and quantitatively analyze micro-irradiation experiments in live cells.

We identified the recruitment kinetics of the central BER/SSBR factors Polβ and XRCC1, confirming that Polβ recruitment was attenuated in XRCC1-KO cells and dependent on its V303 loop to bind to XRCC1, as previously described (Figure 4C) (Fang et al., 2014). Interestingly, we observed Polβ dissociating from the repair complex before XRCC1 (Figures 1B and 1C). We considered that overexpression of the enzymatic component of the repair complex (EGFP-Polβ) might enable faster repair of DNA damage when compared to cells with lower levels of the EGFP-Polβ fusion protein. It is unknown if Polβ and XRCC1 are recruited as a heterodimer to sites of DNA damage or if they combine at the site, but loss of Polβ (via knockout) did not prevent XRCC1's ability to assemble at sites of DNA damage (Figure 4D), implying a stepwise complex-assembly mechanism. Similarly, LIG3 disassembles from sites of DNA damage prior to XRCC1 (Figure 4G). While XRCC1/LIG3 functions as a heterodimer in a similar manner to XRCC1/Polβ at sites of damage, it is unknown if LIG3 and XRCC1 (or LIG3, XRCC1, and Polβ) are recruited together. In either case, these results suggest that Polβ is being removed from the site prior to XRCC1, which implicates an additional control mechanism for Polβ (and possibly LIG3) repair-complex disassembly.

We found that loss of Polβ enhanced the overall level of XRCC1 recruitment to and the time of retention at sites of laser-induced DNA damage (Figure 4D). Re-expression of Polβ in POLB-KO cells restored XRCC1's assembly/disassembly kinetics (Figures 4E and S7B–S7D). This may be explained by incomplete repair of the damage site due to a lack of Polβ's enzymatic activities. However, neither EGFP-tagged mutants for Polβ's dRP lyase (K72A or K35A/K68A/K72A) nor polymerase (D256A) activities demonstrated altered recruitment kinetics compared to functional Polβ (Figure 3A), even when endogenous Polβ was removed (Figures 3E and 3F), and re-expression of either dRP lyase deficient or polymerase-deficient Polβ restored XRCC1's dissociation profile (Figures S7B–S7D). Together, these results support a model where Polβ recruitment to and dissociation from DNA repair complexes is not dependent on repair of the DNA lesion itself (or repair is

facilitated by compensatory enzymes) and that Polβ promotes removal of XRCC1 from the DNA damage site. This model is further supported by the lack of change observed in assembly/disassembly kinetics between EGFP-Polβ overexpression and endogenously expressed EGFP-Polβ (Figure 2E). Interestingly, LIG3 recruitment kinetics are unchanged in POLB-KO cells (Figure 4G). This also supports a mechanism where LIG3 is removed prior to XRCC1 from sites of DNA damage, even when XRCC1 recruitment is prolonged resulting from the loss of POLB.

Due to the dependence of Polβ and XRCC1 on PAR for recruitment, we investigated the role of PAR on recruitment dynamics. We developed a live-cell probe for poly(ADP-ribose), herein termed LivePAR (a PBD-GFP fusion using the WWE domain from the PAR-binding protein RNF146) to provide real-time, live-cell imaging of PAR formation at sites of laser micro-irradiation (Figures 1D and 1E). LivePAR's focal recruitment is dependent on its ability to bind PAR and, as we show, does not require BrdU or Hoechst sensitization for recruitment visualization using either 355-nm or 405-nm laser wavelengths. We directly compared it to other PBD fusion proteins and found that the intensity of LivePAR recruitment was 13-fold greater than the H2A1.1 macrodomain and 7-fold greater than XRCC1's BRCT1 domain (Figures S2E–S2G). LivePAR is responsive and readily resolves at micro-irradiation settings that elicit Polβ and XRCC1 recruitment, two factors whose recruitment is dependent on PAR formation. PARP1/PARP2 inhibition prevented PAR formation at sites of laser-induced DNA damage and was required for Polβ and XRCC1 recruitment, while loss of PAR degradation enhanced retention of Polβ and XRCC1 at sites of damage (Figures 5C and 5D). These experiments confirmed that the presence of PAR at sites of DNA damage is a critical step for Polβ and XRCC1 recruitment and regulates complex retention kinetics.

One caveat of overexpressing PBD fusion proteins such as LivePAR is the possibility of impeding recruitment of endogenous PAR-binding proteins. LivePAR-expressing cells showed lower PAR immunofluorescence intensity, suggesting that the LivePAR probe and the PAR antibody are competing for binding to PAR (Figure S3C). Similarly, other endogenous PAR-binding proteins, such as XRCC1, may exhibit lower PAR-binding capacity when LivePAR is greatly overexpressed. Molecularly, we anticipate that LivePAR binds to available iso-ADP-ribose moieties within PAR chains that are not occupied by endogenous proteins when expressed at low enough levels but may become intrusive during DNA repair when expressed above a certain threshold. This in turn may lead to altered DNA repair in LivePAR-expressing cells, and this caveat should be considered when utilizing the LivePAR probe. Interestingly, the disruption of PAR-binding proteins is relevant to prolonged XRCC1 retention in POLB-KO cells (Figure 4E). By increasing XRCC1 retention, other PAR-binding proteins may exhibit reduced binding to PAR during DNA damage, leading to disruption of PAR-associated BER/SSBR repair or DSBR that initiates after BER/SSBR fails.

We investigated how loss of Polβ or of XRCC1 affected PARP1 and PARP2 recruitment, as BER status has been implicated in PARP inhibitor sensitivity (Horton et al., 2014). Both POLB-KO and XRCC1-KO cells displayed altered PARP1 recruitment (Figures S8A and S8B). Interestingly, PARP2 showed prolonged retention in XRCC1-KO cells, while loss

of Polβ did not alter PARP2 recruitment, suggesting that PARP1 and PARP2 recruitment kinetics to sites of DNA damage are differentially regulated by cellular levels of Polβ and XRCC1. PARP1 retention could be explained by loss of Polβ alone, and PARP1 recruitment would behave similarly in XRCC1-KO cells, because XRCC1 attenuates Polβ recruitment to DNA damage, thereby reducing Polβ at foci (Figures 4B and 4C). The prolonged PARP1 retention in POLB-KO cells could also explain the retention of XRCC1 in POLB-KO cells, as LivePAR demonstrated enhanced PARylation (Figure 4E) and the addition of a PARP inhibitor following foci formation was able to attenuate XRCC1 retention (Figure S7E). Because PARP2 recruitment was unchanged in POLB-KO cells, the retention of XRCC1 in POLB-KO cells is likely the result of the retention of PARP1, but not PARP2.

NRH supplementation enhanced intracellular NAD^+ in U2OS cells, leading to increased assembly of Polβ/XRCC1 repair complexes (Figure 6). Interestingly, NRH was unable to enhance NAD^+ in A549 cells. Enhancing or depleting NAD^+ can alter Polβ/XRCC1 repair-complex assembly and the PARylation-dependent BER/SSBR response following genotoxic stress, in agreement with previous reports (Saville et al., 2020; Wilk et al., 2020). For example, reduced intracellular NAD^+ following FK866 inhibition reduces the ability of cells to repair methyl methane sulfonate (MMS)-induced DNA damage, primarily repaired by BER (Wilk et al., 2020). Further, enhancing intracellular NAD^+ using NRH protects cells treated with either MMS or H_2O_2, both of which produce DNA damage repaired by BER/SSBR (Yang et al., 2019). Our findings support NAD^+ supplementation as a mechanism to promote DNA damage repair via PAR-mediated BER/SSBR.

Finally, we utilized our Polβ/XRCC1/LivePAR system to characterize how deficiency of SIRT6 leads to compromised BER. We found that SIRT6-KO does not alter PAR formation following micro-irradiation, but XRCC1 recruitment is attenuated (Figure 7). These results implicate SIRT6 in enhancing the localization of XRCC1 to sites of DNA damage, and SIRT6 loss diminishes the ability of XRCC1 to bind to PAR or to be retained at sites of PARylation. Due to the dependence of Polβ on XRCC1 for repair-complex assembly, we predicted that Polβ recruitment to sites of DNA damage would diminish in the absence of SIRT6, as demonstrated (Figure 7B). Re-expressing catalytically inactive forms of SIRT6 rescued this phenotype, suggesting a role of SIRT6 in regulating this complex, possibly via a structural role or a cryptic enzymatic function. These results would explain the observations from previous studies where enhancing Polβ dRP lyase activity reduces genotoxic sensitivity to SIRT6 loss (Mostoslavsky et al., 2006). Due to the importance of XRCC1 to serve as a scaffold for multiple DNA repair enzymes (e.g., Polβ, PNKP, APLF, APTX, and LIG3) at sites of DNA damage, these results suggest that SIRT6 regulates multiple DNA repair enzymes in BER and SSBR.

STAR★METHODS

RESOURCE AVAILABILITY

Lead contact—Further information and requests for resources and reagents, including custom analysis scripts, should be directed to and will be fulfilled by the lead contact, Robert W. Sobol (rwsobol@southalabama.edu).

Materials availability—Plasmids generated in this study have been deposited to Addgene, with name and catalog numbers available in the key resources table above. All unique/stable reagents generated in this study are available from the Lead Contact with a completed Materials Transfer Agreement.

Data and code availability—All data reported in this paper will be shared by the lead contact upon request. All original code (MIDAS) has been deposited in a GitHub repository (Zenodo) and is publicly available as of the date of publication. DOIs are listed in the key resources table. Any additional information required to reanalyze the data reported in this paper is available from the lead contact upon request.

EXPERIMENTAL MODEL AND SUBJECT DETAILS

The human tumor cell lines A549 and U2OS were obtained from ATCC and are routinely validated by Genetica Cell Line Testing. Human tumor cell lines were modified by lentiviral-mediated expression of the indicated proteins as detailed below and as listed in Table S4 and the key resources table above. In some cases, modified cells were iteratively modified by a second transduction, such as expressing POLB-KO-gRNA in cells followed by expression of EGFP-Polβ-PAMMut using lentiviral vectors with different selection makers (Puromycin, Hygromycin). Lentiviral constructs containing EGFP or mCherry fused to POLB, XRCC1 and PAR binding domains were generated for visualization of protein recruitment to sites of laser-induced (micro-irradiation) DNA damage. Genomic modification of A549 cells to introduce EGFP into the endogenous POLB gene was used for visualization of Polβ protein recruitment with laser-induced micro-irradiation experiments when evaluating endogenous protein expression levels. Several CRISPR/Cas9 KO vectors were used to establish the effect of the targeted protein loss on the recruitment of EGFP or mCherry-fused DNA repair proteins to sites of laser-induced (micro-irradiation) DNA damage. All parental and modified cell lines were cultured in tissue culture incubators at 37°C, 10% CO_2.

METHOD DETAILS

Chemicals and Reagents—All chemicals and reagents used for these experiments are listed in the key resources table. FK866 (NIMH #F-901; IUPAC name: (E)-[4-(1-Benzyoylpiperidin-4-yl)butly]-3-(pyridin-3-yl)acrylamide; CAS number: 201034–75-5) was obtained from the National Institute of Mental Health Chemical Synthesis and Drug Supply Program (Bethesda, MD). FK866 was dissolved in DMSO to prepare a stock solution at a concentration of 1 mM and stored at −80°C. Dihydronicotinamide Riboside (NRH; 1-[(2R,3R,4S,5R)-3,4-Dihydroxy-5-(hydroxymethyl)tetrahydrofuran-2-yl]-4H-pyridine-3-carboxamide) was prepared as described (Giroud-Gerbetant et al., 2019). NRH was dissolved in distilled H_2O to prepare a stock solution (100mM) and stored at −80°C.

Plasmid and vector development—Plasmids and lentiviral vectors developed previously or those newly generated for this study, either obtained commercially or from colleagues, are all cited in the key resources table above. Lentiviral vectors were prepared by VectorBuilder Inc. unless specifically stated below. pLV-EGFP-Polβ-hygro-PAMmut, pLV-

EGFP-Polβ(K72A)-hygro-PAMmut, and pLV-EGFP-Polβ(D256A)-hygro-PAMmut were created by mutating nucleotide G24 in POLB (located in the sequence corresponding to exon 1) to G24A with the Quickchange II XL site-directed mutagenesis kit and the primers listed in the Table S5 to generate PAM mutants resistant to CRISPR/Cas9 cleavage by POLBKO-gRNA1. Positive clones were selected and plasmids were extracted with the QIAprep Spin Miniprep Kit (QIA-GEN). Modifications were verified by Sanger sequencing (Eurofins Genomics). The pLVX-CMV-XRCC1-gRNA-res-Neo vector was created by purchasing a pENTR-XRCC1-gRNA-Res construct (Genscript USA, Inc.) with a mutated nucleotide G81A in XRCC1 (located in the sequence corresponding to exon 2) to generate PAM mutants resistant to CRISPR/Cas9 cleavage by XRCC1-gRNA1, and then Gateway cloning into a Gateway-modified pLVX-CMV-Neo vector.

The generation of the pUC19-POLBHR-EGFP insert used for endogenous tagging of the N terminus of POLB in A549 cells began with modification of a commercially available pUC19 plasmid (NEB) to remove a SapI restriction site using the QuikChange II XL kit and PCR primers (see Table S5 - primers 1433 & 1434). Following clonal selection, the resulting plasmid was then modified to insert a ~1.7kb high-fidelity PCR-amplified homology region fragment of POLB (including part of exon 1) generated using A549 genomic DNA as the template (primers 1427 & 1428). Following clonal selection, the resulting plasmid was modified to remove the PAM site in POLBHR used by the targeting CRISPR gRNA. Following clonal selection, the plasmid was modified via site-directed mutagenesis to add a SapI site located at the transcription start site of POLB (primers 1435 & 1436). An oligonucleotide was generated by high-fidelity PCR to contain SapI restriction fragments on the ends flanking the EGFP cDNA (primers 1437 & 1438). Lastly, the pUC19-POLBHR plasmid was modified to insert the SapI-EGFP DNA fragment via restriction digestion and ligation at the SapI site to produce a final pUC19 vector (pUC19-POLBHR-EGFP) with a ~2.5kb insert containing ~800bp upstream homology arm, EGFP in frame with the transcription start site of POLB, a PAM mutation in exon 1 to prevent secondary cleavage by CRISPR/Cas9, and ~800bp downstream EGFP-POLB (see Figure 2A). The entire insert was sequenced via Sanger sequencing (Eurofins Genomics) to ensure proper generation and sequence validation.

Generation of constructs containing PAR binding domains (PBD) fused to EGFP began with a commercially purchased lentiviral backbone vector (VectorBuilder Inc.) containing a Gly-Ser linker, an EGFP open reading frame and MluI and BamHI restriction sites to enable in-frame cloning of the PBD (pLV-Hygro-EF1A-LivePARBackbone). DNA fragments containing each of the PBD sequences were generated by GenScript USA, Inc (see Table S1). PBD cDNA was amplified by high-fidelity PCR (primers 1485 & 1486). Each PBD-containing DNA fragment was ligated into the restriction-digested backbone vector and clonally selected.

Lentivirus production and cell transduction—Lentiviral particles were generated by co-transfection of 4 plasmids into 293-FT cells using TransIT-X2 Transfection reagent: the packaging vectors pMD2.g(VSVG), pVSV-REV and pMDLg/pRRE together with the appropriate shuttle vectors, as listed in the key resources table above. Forty-eight hours after transfection, lentivirus-containing supernatant was collected and passed through 0.45 mM

filters to isolate the viral particles as described previously (Fang et al., 2014; Fouquerel et al., 2014).

Lentiviral transduction was performed as follows: cells ($1–2\times10^5$) were seeded into 6-well plates. 24 hr later, lentiviral particles (1ml) were mixed with polybrene (2μg/ml) and added to the cells. Cells were incubated at 32°C overnight and then medium with lentiviral particles was removed and replaced with fresh medium. When cells were created to form stable cell lines, cells were cultured for 48 hr at 37°C before selection with antibiotics (puromycin or hygromycin) for 1–2 weeks. When cells were transduced a second time to create a cell expressing a fluorescently tagged fusion protein in addition to harboring a KO, selection for the first stable cell line was completed and verified prior to initiation of the second transduction. When cells were created (transduced) for transient expression experiments, cells were cultured for at least 96 hr, but no more than two weeks, at 37°C before experimental analysis. All stable cell lines developed and used in this study (along with media formulations) are listed in Table S4.

Development of Cas9 expressing and knockout (KO) cells—We developed U2OS and A549 cell lines with stable knockouts using the one vector CRISPR/Cas9 system (plentiCRISPR-v2; to deliver hSpcas9 and puromycin resistance). The plentiCRISPR-v2 vector was obtained from Addgene (plasmid #52961). The plentiCRISPR-v2 vectors containing control gRNA, POLB-KO-g2, XRCC1-KO-g1, XRCC1-KO-g2 and PARP1-KO-g1 were gifts from Wim Vermeulen (Erasmus MC, the Netherlands) (Slyskova et al., 2018). To generate plentiCRISPR-v2 containing gRNAs for POLB (using gRNA1), TARG, or SIRT6, we designed the guide RNA (gRNA) using the ChopChop software package (http://chopchop.cbu.uib.no). The resulting gRNAs (and the oligonucleotides used to generate the vectors) are listed in the Table S5. The plasmids were used to generate lentivirus for expression of Cas9+Control-gRNA or Cas9+KO-gRNA, and U2OS or A549 cells were transduced with lentivirus as indicated above. Cells were maintained in media containing puromycin (1 μg/ml) for 16 days, plated to generate single cell derived colonies, and validated by sequencing and protein immunoblot to confirm the knockout. Details of the technique have been described by us previously (Fang et al., 2019) and earlier by others (Sanjana et al., 2014).

Generation of A549 cells expressing endogenous EGFP-tagged Polβ—Prior to use, the entire 2.5kb POLBHR-EGFP insert utilized for HR-dependent EGFP modification of the POLB gene was enzymatically cleaved from the pUC19 backbone and gel purified to be used for CRISPR/Cas9 ribonucleoprotein complex mediated insertion as below. To modify A549 cells to express EGFP-Polβ under control of the endogenous POLB promoter, the protocol provided by IDT was followed with minimal changes. First, tracrRNA (100 μM) and POLB gRNA1 (100 μM) were mixed with room temperature PBS, heated to 95°C, and then cooled slowly to room temperature. Cas9 protein was diluted to a concentration of 1 μM with room temperature PBS and then combined with the tracrRNA:POLBgRNA1 duplex to form the ribonucleoprotein complex in OptiMEM at room temperature for 5 minutes. The ribonucleoprotein complex was treated with RNAiMAX in OptiMEM for 20 minutes at room temperature to facilitate cellular delivery. During this time, the

2.5kb POLBHR-EGFP DNA fragment was treated with TransIT-X2 in Opti-MEM at room temperature for 15 minutes. Finally, A549 cells were trypsinized and reseeded to 5×10^5 cells per well in a 6-well dish, followed by addition of the Cas9 ribonucleoprotein complex and the 2.5kb POLBHR-EGFP DNA fragment. Cells were incubated for 48 hours, at which time the cells were trypsinized and reseeded into glass-bottom 96-well dishes at 3 cells/mL, 100 μL per well. Single cell clones were grown until visible colonies could be observed. Individual colonies were visualized for EGFP fluorescence using a Nikon A1rsi laser scanning confocal microscope to verify positive EGFP fluorescence. Positive colonies were trypsinized and grown for validation of CRISPR/Cas9-mediated modification of the POLB gene.

In addition to immunoblots and spectral immunofluorescence of EGFP-Polβ (methods below), Sanger sequencing was performed to verify correct insertion of EGFP within and in-frame of the POLB gene. Genomic DNA from A549/POLBHR-EGFP cells was isolated, and the genomic region around the fragment insert site was PCR amplified using high-fidelity PCR and PCR-primers containing HindIII and EcoRI restriction fragments on the ends (see Table S5 - primers 1427 & 1428). The PCR product was ligated into pUC19, transformed into STBL3 bacteria, and plated to obtain single colonies. Individual bacterial colonies were selected, and plasmids were isolated and sequenced completely across the POLBHR region to identify modifications in the POLBHR sequence. All three A549 POLB alleles were sequenced (see Table S2). Following validation, one cell clone was amplified and utilized for experimental investigation.

Cell protein extract preparation—Protein extracts (whole cell lysates, WCL) were prepared from cells with different genetic modifications and/or treated with different drugs and for different times as indicated in the text. Cells were seeded into a 60-mm cell culture dish. After reaching 75%–80% confluency, cells were washed twice with cold PBS, collected and lysed with an appropriate volume of 2x clear Laemmli buffer (2% SDS, 20% glycerol, 62.5mmol/l Tris-HCl pH6.8). Cell lysates were boiled for 10 min and quantified with the DC protein assay kit following the microplate protocol provided by the company (Bio-Rad).

Immunoblot—Whole cell protein lysates (15–40 μg protein) were loaded onto precast NuPAGE® Novex® 4%–12% Bis-Tris gels, run 1hr at 120V. Gel electrophoresis separated proteins were transferred onto a PVDF membrane or nitrocellulose membrane using a Turboblotter (Bio-Rad). The membrane was first blocked with B-TBST (TBS buffer with 0.05% Tween-20 and supplemented with 5% blotting grade non-fat dry milk; Bio-Rad) for 1 hr at room temperature and subsequently blotted with the primary antibodies in B-TBST overnight at 4°C. The primary antibodies and their dilutions are listed in the key resources table. After washing, membranes were incubated with secondary antibodies in B-TBST for 1 hr (room temperature). The following HRP conjugated secondary antibodies were used: Bio-Rad Goat anti-mouse-HRP conjugate and Bio-Rad anti-rabbit-HRP conjugate (see key resources table). After washing, the membrane was illuminated with a chemiluminescent substrate. Protein bands were imaged using a Bio-Rad Chemi-Doc MP imaging system.

Cell treatment, lysate preparation, and immunoblot analysis for PAR detection —U2OS or LN428 cells were seeded in 100mm plates at a density of 5.0×10^5 cells/well and allowed to culture overnight (18 hr). Cells were then treated with FK866, NRH, ABT-888 or H_2O_2 as indicated in the figure legends and as follows: For FK866 treatments, cells were treated with FK866 (50 nM) and cultured for another 24 hr before lysis; for NRH treatments, cells were treated with NRH (100 μM) for 4 hr before lysis; for ABT-888 treatments, cells were treated with ABT-888 (10 μM) for 1 hr before lysis and for H_2O_2 treatments, cells were treated with H_2O_2 (100 μM or 300 μM) for 15 mins before lysis. To prepare PAR-stable whole cell lysates, cells were washed 3x with cold PBS and lysed in 500 μL of 2x clear Laemmli buffer (2% SDS, 20% glycerol, 62.5mmol/l Tris-HCl pH6.8). Cell lysates were then heated at 95°C for 10 mins followed by centrifugation for 5 mins at 1200 rpm. Immunoblot samples were prepared in a 1:1 ratio with 2x blue Laemmli buffer (2x clear Laemmli buffer + 0.005% bromophenol blue) and heated for an additional 5 minutes at 95°C followed by centrifugation for 5 minutes at 1200 rpm. Lysates (30 μg protein) were loaded on a 15-well NuPAGE, Novex 4%–12% Bis-Tris gel, and allowed to run for 1 hr at 120V. Gel electrophoresis separated proteins were transferred onto a nitrocellulose membrane using a Turboblotter (Bio-Rad). The nitrocellulose membrane was placed on a rocker in blocking buffer (TBST + 5% milk) at room temperature for 30 mins. The membrane was then incubated in PAR antibody (1:1000) diluted in blocking buffer overnight at 4°C. The primary antibodies and their dilutions are listed in the key resources table. The following day, the membrane was washed 3x in TBST (5 min) and the secondary antibody was allowed to incubate on the membrane at room temperature for 2 hr. The following HRP conjugated secondary antibody was used: Bio-Rad Goat anti-mouse-HRP conjugate (see key resources table). After washing, the membrane was illuminated with a chemiluminescent substrate. Protein bands were imaged using a Bio-Rad Chemi-Doc MP imaging system.

MIDAS—MIDAS (for **M**odular **I**rradiation, **D**etection, and **A**nalysis **S**ystem) is a flexible, user-friendly, and integrated software platform for start-to-finish performance and statistical analysis of micro-irradiation experiments. It is **M**odular in that each component offers the user multiple complementary approaches that may be freely combined. The **I**rradiation component is currently implemented as a macro written for NIS-Elements, which provides a graphical user interface (GUI) for choosing settings for laser wavelength, power, irradiation pattern(s), and image acquisition. Irradiation patterns and image acquisition can be tailored for time-lapse video of live cells expressing fluorescently labeled molecules of interest, for fixative-based staining following irradiation, or for combined approaches. Time-lapse irradiation experiments can be performed in parallel, with multiple cells in a single field being irradiated and then imaged collectively, or in series, where a selected group of cells are stimulated and imaged in sequence. Both approaches irradiate cells sequentially - the parallel module measures the duration of each irradiation event and applies a per-cell timing offset to accurately measure time post-irradiation when imaged. For fixative-based staining, a custom image registration algorithm is used to precisely re-locate the image field following sample preparation. After irradiation and image acquisition, the **D**etection component guides the user through the semi-automated measurement process, allowing for user supervision, and intervention, if necessary, while easing workflow by automating

repetitive tasks. This component is implemented as a script for FIJI written in the Jython language, and features modes for measuring serial video, parallel video, or individual stained images. After data have been measured and output to a summary file, the **A**nalysis component is used for visualization and statistical analysis of multiple datasets, as a final step for the overall **S**ystem. This component is written in Python, using the Matplotlib and Numpy libraries for data processing. Data can be viewed at single-cell resolution or as averaged populations, with multiple normalization options to foreground different aspects of the data: normalized to a reference to minimize cell-to-cell variability, normalized to per-cell maximum intensity to emphasize differences in timing, and normalized to a pre-irradiation image to emphasize differences in intensity. To quantitatively assess features of recruitment data, three measurements are made for each intensity trace: time to peak recruitment intensity, half-life of recruitment, and relative peak intensity. Time to peak is defined as the time at which recruitment intensity crosses a threshold set to the 95% confidence interval of the maximum intensity for that cell. Half-life of recruitment is defined as the time post-peak at which the intensity crosses a lower threshold set to the same confidence interval of 50% of the maximum intensity. Relative peak intensity is defined as the ratio of maximum intensity per cell to the pre-irradiation intensity of that cell. Data are then analyzed statistically, and standard errors of the mean are reported. For record keeping and downstream analysis/visualization, an Excel format spreadsheet is generated, including all raw data, normalizations, measured features, statistical analyses, and experimental settings. To ensure data integrity and record keeping, although data may be excluded from analyses by the user, these data are still included in the summary spreadsheet, although plainly marked as excluded from analysis. MIDAS was developed and implemented at the USA Mitchell Cancer Institute (J.F.A.), with invaluable conceptual input from Dr. Natalie Gassman.

Laser micro-irradiation—For laser micro-irradiation, 5×10^4 cells were seeded into each well of an 8-chamber glass bottom vessel (Thermo Fisher Scientific, #155409). 24 hours later, laser micro-irradiation was performed using a Nikon A1r confocal microscope. For photo-sensitization experiments involving bromodeoxyuridine (BrdU), cell media was replaced with fresh media containing 10 μM BrdU, and cells were incubated for an additional 24 hours. Live cells were imaged with a Nikon A1rsi laser scanning confocal microscope equipped with 6 visible wavelength lasers (405, 441, 514, 561, 647nm, Coherent), customized to add a UVA 355nm laser (PicoQuant) controlled by a Brueker XY Galvanometer, and equipped with a live-cell incubation chamber (Tokai Hit) maintained at 5% CO_2 and 37°C, using a 20x (NA = 0.8) non-immersion objective or 40x (NA = 1.4) oil-immersion objective for 405 nm or 355 nm laser micro-irradiation, respectively. A 355nm laser or a 405nm laser (as indicated) was used for micro-irradiation, with stimulation times varying from 1–2.5 s per site for the 355nm laser and 0.125–0.25 s per site for the 405nm laser. For parallel irradiation, time lapse images were collected every 15 s during a 10–20 min interval, while an interval of 250ms and a duration of 1 minute were used for serial irradiation. Images of focal recruitment were quantified using MIDAS for quantitation of and statistical analysis of focal recruitment. Forty individual cells (2 sets of 10 cells were performed on 2 separate days) were analyzed and used to generate recruitment profiles and kinetic parameters.

Generation of PAR binding domain (PBD) fusion constructs and cells—A lentiviral backbone vector (pLV-Hygro-EF1A-LivePARBackbone) was generated to include MluI and BamHI cloning sites 3′ to the EF1A promoter and Kozak sequence but 5′ to a 3xGGGS linker followed by EGFP. DNA fragments encoding an individual PAR binding domain (PBD; Table S1) along with a 5′ terminal MluI site and a 3′ terminal BamHI site were purchased from Genscript or Twist Biosciences. The backbone vector and each PBD were dual restriction digested with MluI and BamHI, and individual PBDs were ligated using T7 DNA ligase into the backbone vector, resulting in a PBD-EGFP fusion vector which was transformed into STBL3 bacteria for plasmid amplification. Each resulting PBD-EGFP vector was Sanger sequenced to ensure cloning fidelity. For cell expression, A549 cells were transduced with lentivirus derived from each PBD-EGFP vector as described above, and cells were selected with hygromycin to generate stable cell lines. EGFP fluorescence was visually confirmed by confocal microscope. To test the recruitment of the PBD-EGFP fusions to sites of DNA damage induced by laser micro-irradiation, A549/PBD-EGFP expressing cells were laser micro-irradiated at each of the following conditions: 1) 355nm laser for 2.5 s; 2) 355nm laser for 2.5 s following photo-sensitization (24 hour pre-treatment with BrdU, 10 μM); 3) 405nm for 0.125 s; 4) 405nm for 0.125 s following photo-sensitization (24 hour pre-treatment with BrdU, 10 μM). At least 10 cells from each A549/PBD-EGFP expressing cell line were tested under each micro-irradiation condition to identify focal recruitment during a 10-minute window. Of all PBD-EGFP constructs tested, only four (WWE-EGFP, XL1/BRCT1-EGFP, BRCT1-EGFP, and Macrodomain-EGFP) recruited to at least one of the four conditions.

Immunofluorescence confocal microscopy—For immunofluorescence analysis of poly(ADP-ribose) (PAR) or γH2AX in micro-irradiated cells, 5×10^4 cells were seeded into each well of an 8-chamber cover-glass bottom vessel (Thermo Fisher Scientific, #155409). Cells were laser micro-irradiated using a Nikon A1rsi laser scanning confocal microscope at 355nm or 405nm with either a 20x (NA = 0.8) non-immersion objective or 40x (NA = 1.4) oil-immersion objective, respectively, then subsequently fixed with 4% PFA for 10 min and permeabilized with a 0.1% Triton X-100 solution in PBS for 10 min. Cells were rinsed with PBS and blocked in blocking buffer (10% normal goat serum in PBS) for 30 min and subsequently incubated with the PAR or γH2AX primary antibodies for 2 hr at room temperature, followed by three PBS washes and incubation with both a goat anti-mouse antibody conjugated to Alexa 568 and a goat anti-rabbit antibody conjugated to Alexa 647 (see key resources table for primary and secondary antibodies used, with dilutions for each). Nuclei were stained with DAPI (NucBlue Fixed, Thermo Fisher Scientific, #R37606). Fixed cells were imaged with a Nikon A1r laser scanning confocal microscope, using a 20x or 40x oil-immersion objective, as above.

Fluorescent Recovery After Photobleaching (FRAP)—For FRAP experiments, 5×10^4 cells were seeded into each well of an 8-chamber cover-glass bottom vessel (Thermo Fisher Scientific, #155409). 24 hours later, cells were imaged using a Nikon A1r laser scanning confocal microscope using a 60x oil-immersion objective (NA 1.4), with a stage-top incubation chamber. To achieve high temporal resolution a field of 64×32 pixels (0.41 μm/pixel) was imaged. Pre-bleach images were acquired for a duration of 8 s at a frame rate

of 35ms. Photobleaching was achieved using a 488nm laser set to 100% power for 12.5ms bleaching across a 64×6 pixel rectangle across the middle of a cell's nucleus. Post-bleach images were then acquired for an additional 30 s using a 35ms interval. At least 15 cells were photobleached and imaged for each experimental session, and at least two sessions were performed for each condition. For quantitation, a 6×6 pixel square ROI was quantitated inside the 64×6 pixel bleaching window, with total fluorescent intensity obtained for each image within the ROI. The initial fluorescent intensity (F_i) of the ROI was calculated as the average intensity of the ROIs of 40 frames taken 1.2 s before photobleaching. The fluorescent intensity after photobleaching (F_0) was the fluorescent intensity of the ROI in the first frame immediately after photobleaching. The recovered fluorescent intensity (F_r) was the average intensity of the ROIs of 100 frames taken 13–16.5 s after photobleaching, after a noticeable plateau had formed. The mobile fraction (MF) was calculated by: $MF = (F_r - F_0)/(F_i - F_0)$.

Cell proliferation and cell doubling time analysis—Cells were plated into a 96-well dish at a density of 1×10^4 cells per well, with 6 wells per cell line assayed. Cells were fixed at 24, 48, 72, and 96 hr using 4% paraformaldehyde containing 20 μM Hoechst 33342 dye. Cell nuclei were imaged and counted using a Celigo S Imaging Cytometer (Nexcelom Bioscience). Cell counts were normalized to the average number of cells at 24 hr for a given cell line. Cell doubling times (DT) were calculated for each 24 hr interval (i.e., 24 to 48 hr, 48 to 72 hr, and 72 to 96 hr) using the following equation: DT = 24*ln(2) / ln(normalized final cell number / normalized initial cell number). The cell doubling times for each interval were averaged to create a mean doubling time for each cell line. The assay was repeated in duplicate.

Cell cycle analysis—Cells were trypsinized and plated in a 100mm dish at 5×10^5 cells per dish. Cells were allowed to grow to a maximum of 50% confluence, at which point the cells were trypsinized, centrifuged, and washed twice with ice-cold 1X PBS. Pelleted cells were resuspended in 70% ice-cold ethanol and stored at 4°C for no more than a week. On the day of analysis, cells were centrifuged, washed twice with ice-cold 1X PBS, and resuspended in 1X PBS at a density of 1×10^6 cells/ml. Cells were treated with 5 μg RNase and incubated at 37°C for 30 minutes. Propidium iodide was added to the cells at a final concentration of 50 μg/mL, and cells were incubated for 20 mins at room temperature. Data was acquired on a BD FACS Canto II cytometer running Diva V 8.3 software (BD Biosciences, San Jose, CA). Cell cycle modeling was performed using Modfit LT Software V4.1 (Verity Software House, Topsham, ME).

Spectral imaging of A549/POLβHR-EGFP cells—For spectral separation of low intensity EGFP visualization, spectral images were obtained with a Nikon A1rsi laser scanning confocal microscope using 488 nm laser for excitation and collecting 14 bands from 500.2nm to 638.4nm, with a spectral gating resolution set to 10nm. Spectra were collected from parental and A549/EGFP-Polβ cells to provide spectra for autofluorescence and EGFP, respectively. Spectral unmixing was performed in NIS-Elements.

NAD+/NADH analysis—The cellular level of NAD^+ and NADH was measured using the Enzychrome NAD^+/NADH colorimetric assay kit (BioAssay Systems), following the supplier-provided protocols with minimal changes, as we have described previously (Wilk et al., 2020). Cells were seeded in a 6-well plate at a density of 2×10^5 cells per well for NAD^+ measurements and 3×10^5 cells per well for NAD^+ pool measurements (NAD^+ plus NADH). 24 hr later, cells were treated with NRH (100 μM) for 0, 0.5, 1, 2, 4, 8 and 24 hr or with FK866 (50nM) for 24 hours. Following treatment, cells were harvested and a suspension of 2×10^5 cells was divided in half for measuring NAD^+ and NADH, respectively, or a suspension of 1×10^5 cells was used for the NAD^+ measurement only. Cell pellets were immediately homogenized using plastic pestles and the extraction of NAD^+ and NADH was performed in the provided lysis buffers. Extracts were heated at 60°C for 5 min and neutralized with the provided buffers. Samples were spun down and the supernatant was immediately used for measurements of NAD^+/NADH content using a Microplate Reader (BioTek) at 565 nm.

QUANTIFICATION AND STATISTICAL ANALYSIS

Averages and standard error of the mean (SEM) were calculated from the means (on technical replicates) of multiple independent experiments (n = number of independent experiments as indicated in figure legends) unless stated otherwise. Student t test and ANOVA was used to test for significant differences as appropriate, with results generally compared to controls and as indicated in the figure legends. P values are indicated by asterisks with: *$p < 0.05$, **$p < 0.01$, ***$p < 0.001$, ****$p < 0.0001$. Statistical analyses were performed using GraphPad PRISM except those explicitly determined in MIDAS.

Supplementary Material

Refer to Web version on PubMed Central for supplementary material.

ACKNOWLEDGMENTS

R.W.S. is an Abraham A. Mitchell Distinguished Investigator. Research in the Sobol lab on DNA repair, the analysis of DNA damage, and the impact of genotoxic exposure is funded by the National Institutes of Health (NIH) (grants CA148629, ES014811, ES029518, ES028949, and CA238061), the National Science Foundation (NSF) (grant NSF-1841811), and the DOD (grant 11998991, DURIP-Navy). Support is also provided by the Abraham A. Mitchell Distinguished Investigator Fund and the Mitchell Cancer Institute Molecular & Metabolic Oncology Program Development Fund (R.W.S.). Support for the development of LivePAR was also provided by the Mitchell Cancer Institute Junior Faculty Award (to C.A.K.). We thank Dr. Natalie Gassman (UAB) for her invaluable conceptual input on the development of the MIDAS software platform.

REFERENCES

Abbotts R, and Wilson DM 3rd. (2017). Coordination of DNA single strand break repair. Free Radic. Biol. Med 107, 228–244. [PubMed: 27890643]

Almeida KH, and Sobol RW (2007). A unified view of base excision repair: lesion-dependent protein complexes regulated by post-translational modification. DNA Repair (Amst.) 6, 695–711. [PubMed: 17337257]

Beard BC, Wilson SH, and Smerdon MJ (2003). Suppressed catalytic activity of base excision repair enzymes on rotationally positioned uracil in nucleosomes. Proc. Natl. Acad. Sci. USA 100, 7465–7470. [PubMed: 12799467]

Breslin C, Hornyak P, Ridley A, Rulten SL, Hanzlikova H, Oliver AW, and Caldecott KW (2015). The XRCC1 phosphate-binding pocket binds poly (ADP-ribose) and is required for XRCC1 function. Nucleic Acids Res 43, 6934–6944. [PubMed: 26130715]

Chiarugi A, Dölle C, Felici R, and Ziegler M (2012). The NAD metabolome–a key determinant of cancer cell biology. Nat. Rev. Cancer 12, 741–752. [PubMed: 23018234]

Cole HA, Tabor-Godwin JM, and Hayes JJ (2010). Uracil DNA glycosylase activity on nucleosomal DNA depends on rotational orientation of targets. J. Biol. Chem. 285, 2876–2885. [PubMed: 19933279]

Dantzer F, de La Rubia G, Ménissier-De Murcia J, Hostomsky Z, de Murcia G, and Schreiber V (2000). Base excision repair is impaired in mammalian cells lacking Poly(ADP-ribose) polymerase-1. Biochemistry 39, 7559–7569. [PubMed: 10858306]

El-Khamisy SF, Masutani M, Suzuki H, and Caldecott KW (2003). A requirement for PARP-1 for the assembly or stability of XRCC1 nuclear foci at sites of oxidative DNA damage. Nucleic Acids Res 31, 5526–5533. [PubMed: 14500814]

Ensminger M, Iloff L, Ebel C, Nikolova T, Kaina B, and Löbrich M (2014). DNA breaks and chromosomal aberrations arise when replication meets base excision repair. J. Cell Biol 206, 29–43. [PubMed: 24982429]

Fang Q, Inanc B, Schamus S, Wang XH, Wei L, Brown AR, Svilar D, Sugrue KF, Goellner EM, Zeng X, et al. (2014). HSP90 regulates DNA repair via the interaction between XRCC1 and DNA polymerase β. Nat. Commun 5, 5513. [PubMed: 25423885]

Fang EF, Lautrup S, Hou Y, Demarest TG, Croteau DL, Mattson MP, and Bohr VA (2017). NAD^+ in Aging: Molecular Mechanisms and Translational Implications. Trends Mol. Med 23, 899–916. [PubMed: 28899755]

Fang Q, Andrews J, Sharma N, Wilk A, Clark J, Slyskova J, Koczor CA, Lans H, Prakash A, and Sobol RW (2019). Stability and sub-cellular localization of DNA polymerase β is regulated by interactions with NQO1 and XRCC1 in response to oxidative stress. Nucleic Acids Res. 47, 6269–6286. [PubMed: 31287140]

Fouquerel E, and Sobol RW (2014). ARTD1 (PARP1) activation and NAD(+) in DNA repair and cell death. DNA Repair (Amst.) 23, 27–32. [PubMed: 25283336]

Fouquerel E, Goellner EM, Yu Z, Gagné JP, Barbi de Moura M, Feinstein T, Wheeler D, Redpath P, Li J, Romero G, et al. (2014). ARTD1/PARP1 negatively regulates glycolysis by inhibiting hexokinase 1 independent of NAD+ depletion. Cell Rep 8, 1819–1831. [PubMed: 25220464]

Giroud-Gerbetant J, Joffraud M, Giner MP, Cercillieux A, Bartova S, Makarov MV, Zapata-Pérez R, Sánchez-García JL, Houtkooper RH, Migaud ME, et al. (2019). A reduced form of nicotinamide riboside defines a new path for NAD^+ biosynthesis and acts as an orally bioavailable NAD^+ precursor. Mol. Metab 30, 192–202. [PubMed: 31767171]

Holton NW, Andrews JF, and Gassman NR (2017). Application of Laser Micro-irradiation for Examination of Single and Double Strand Break Repair in Mammalian Cells. J. Vis. Exp (127), 56265.

Horton JK, Stefanick DF, Prasad R, Gassman NR, Kedar PS, and Wilson SH (2014). Base excision repair defects invoke hypersensitivity to PARP inhibition. Mol. Cancer Res 12, 1128–1139. [PubMed: 24770870]

Imai S, and Guarente L (2014). NAD+ and sirtuins in aging and disease. Trends Cell Biol 24, 464–471. [PubMed: 24786309]

Jelezcova E, Trivedi RN, Wang XH, Tang JB, Brown AR, Goellner EM, Schamus S, Fornsaglio JL, and Sobol RW (2010). Parp1 activation in mouse embryonic fibroblasts promotes Pol beta-dependent cellular hypersensitivity to alkylation damage. Mutat. Res 686, 57–67. [PubMed: 20096707]

Kubota Y, Nash RA, Klungland A, Schar P, Barnes DE, and Lindahl T (1996). Reconstitution of DNA base excision-repair with purified human proteins: interaction between DNA polymerase β and the XRCC1 protein. EMBO J 15, 6662–6670. [PubMed: 8978692]

Lan L, Nakajima S, Oohata Y, Takao M, Okano S, Masutani M, Wilson SH, and Yasui A (2004). In situ analysis of repair processes for oxidative DNA damage in mammalian cells. Proc. Natl. Acad. Sci. USA 101, 13738–13743. [PubMed: 15365186]

Lee Y, Katyal S, Li Y, El-Khamisy SF, Russell HR, Caldecott KW, and McKinnon PJ (2009). The genesis of cerebellar interneurons and the prevention of neural DNA damage require XRCC1. Nat. Neurosci 12, 973–980. [PubMed: 19633665]

London RE (2015). The structural basis of XRCC1-mediated DNA repair. DNA Repair (Amst.) 30, 90–103. [PubMed: 25795425]

Mao Z, Hine C, Tian X, Van Meter M, Au M, Vaidya A, Seluanov A, and Gorbunova V (2011). SIRT6 promotes DNA repair under stress by activating PARP1. Science 332, 1443–1446. [PubMed: 21680843]

Mao Z, Tian X, Van Meter M, Ke Z, Gorbunova V, and Seluanov A (2012). Sirtuin 6 (SIRT6) rescues the decline of homologous recombination repair during replicative senescence. Proc. Natl. Acad. Sci. USA 109, 11800–11805. [PubMed: 22753495]

Matsumoto Y, Kim K, Katz DS, and Feng JA (1998). Catalytic center of DNA polymerase β for excision of deoxyribose phosphate groups. Biochemistry 37, 6456–6464. [PubMed: 9572863]

Menge KL, Hostomsky Z, Nodes BR, Hudson GO, Rahmati S, Moomaw EW, Almassy RJ, and Hostomska Z (1995). Structure-function analysis of the mammalian DNA polymerase beta active site: role of aspartic acid 256, arginine 254, and arginine 258 in nucleotidyl transfer. Biochemistry 34, 15934–15942. [PubMed: 8519750]

Mesquita I, Varela P, Belinha A, Gaifem J, Laforge M, Vergnes B, Estaquier J, and Silvestre R (2016). Exploring NAD+ metabolism in host-pathogen interactions. Cell. Mol. Life Sci 73, 1225–1236. [PubMed: 26718485]

Montllor-Albalate C, Song Z, and Chen D (2021). The therapeutic promises of NAD^+ boosters. Cell Metab 33, 1274–1275. [PubMed: 34233170]

Mostoslavsky R, Chua KF, Lombard DB, Pang WW, Fischer MR, Gellon L, Liu P, Mostoslavsky G, Franco S, Murphy MM, et al. (2006). Genomic instability and aging-like phenotype in the absence of mammalian SIRT6. Cell 124, 315–329. [PubMed: 16439206]

Rodriguez Y, Howard MJ, Cuneo MJ, Prasad R, and Wilson SH (2017). Unencumbered Pol β lyase activity in nucleosome core particles. Nucleic Acids Res 45, 8901–8915. [PubMed: 28911106]

Rosenstein BS, Setlow RB, and Ahmed FE (1980). Use of the dye Hoechst 33258 in a modification of the bromodeoxyuridine photolysis technique for the analysis of DNA repair. Photochem. Photobiol 31, 215–222. [PubMed: 6154299]

Rouleau M, Patel A, Hendzel MJ, Kaufmann SH, and Poirier GG (2010). PARP inhibition: PARP1 and beyond. Nat. Rev. Cancer 10, 293–301. [PubMed: 20200537]

Sanjana NE, Shalem O, and Zhang F (2014). Improved vectors and genome-wide libraries for CRISPR screening. Nat. Methods 11, 783–784. [PubMed: 25075903]

Saville KM, Clark J, Wilk A, Rogers GD, Andrews JF, Koczor CA, and Sobol RW (2020). NAD^+-mediated regulation of mammalian base excision repair. DNA Repair (Amst.) 93, 102930. [PubMed: 33087267]

Schindelin J, Arganda-Carreras I, Frise E, Kaynig V, Longair M, Pietzsch T, Preibisch S, Rueden C, Saalfeld S, Schmid B, et al. (2012). Fiji: an open-source platform for biological-image analysis. Nat. Methods 9, 676–682. [PubMed: 22743772]

Schreiber V, Amé JC, Dollé P, Schultz I, Rinaldi B, Fraulob V, Ménissier-de Murcia J, and de Murcia G (2002). Poly(ADP-ribose) polymerase-2 (PARP-2) is required for efficient base excision DNA repair in association with PARP-1 and XRCC1. J. Biol. Chem 277, 23028–23036. [PubMed: 11948190]

Sharifi R, Morra R, Appel CD, Tallis M, Chioza B, Jankevicius G, Simpson MA, Matic I, Ozkan E, Golia B, et al. (2013). Deficiency of terminal ADP-ribose protein glycohydrolase TARG1/C6orf130 in neurodegenerative disease. EMBO J 32, 1225–1237. [PubMed: 23481255]

Shi H, Enriquez A, Rapadas M, Martin EMMA, Wang R, Moreau J, Lim CK, Szot JO, Ip E, Hughes JN, et al. (2017). NAD Deficiency, Congenital Malformations, and Niacin Supplementation. N. Engl. J. Med 377, 544–552. [PubMed: 28792876]

Slyskova J, Sabatella M, Ribeiro-Silva C, Stok C, Theil AF, Vermeulen W, and Lans H (2018). Base and nucleotide excision repair facilitate resolution of platinum drugs-induced transcription blockage. Nucleic Acids Res 46, 9537–9549. [PubMed: 30137419]

Sobol RW, Prasad R, Evenski A, Baker A, Yang XP, Horton JK, and Wilson SH (2000). The lyase activity of the DNA repair protein beta-polymerase protects from DNA-damage-induced cytotoxicity. Nature 405, 807–810. [PubMed: 10866204]

Sonavane M, Hayat F, Makarov M, Migaud ME, and Gassman NR (2020). Dihydronicotinamide riboside promotes cell-specific cytotoxicity by tipping the balance between metabolic regulation and oxidative stress. PLoS ONE 15, e0242174. [PubMed: 33166357]

Svilar D, Goellner EM, Almeida KH, and Sobol RW (2011). Base excision repair and lesion-dependent subpathways for repair of oxidative DNA damage. Antioxid. Redox Signal 14, 2491–2507. [PubMed: 20649466]

Tang JB, Goellner EM, Wang XH, Trivedi RN, St Croix CM, Jelezcova E, Svilar D, Brown AR, and Sobol RW (2010). Bioenergetic metabolites regulate base excision repair-dependent cell death in response to DNA damage. Mol. Cancer Res 8, 67–79. [PubMed: 20068071]

Teloni F, and Altmeyer M (2016). Readers of poly(ADP-ribose): designed to be fit for purpose. Nucleic Acids Res 44, 993–1006. [PubMed: 26673700]

The Human Protein Atlas. (2020). http://www.proteinatlas.org.

Tian X, Firsanov D, Zhang Z, Cheng Y, Luo L, Tombline G, Tan R, Simon M, Henderson S, Steffan J, et al. (2019). SIRT6 Is Responsible for More Efficient DNA Double-Strand Break Repair in Long-Lived Species. Cell 177, 622–638.e22. [PubMed: 31002797]

Timinszky G, Till S, Hassa PO, Hothorn M, Kustatscher G, Nijmeijer B, Colombelli J, Altmeyer M, Stelzer EH, Scheffzek K, et al. (2009). A macrodomain-containing histone rearranges chromatin upon sensing PARP1 activation. Nat. Struct. Mol. Biol 16, 923–929. [PubMed: 19680243]

Uhlen M, Zhang C, Lee S, Sjöstedt E, Fagerberg L, Bidkhori G, Benfeitas R, Arif M, Liu Z, Edfors F, et al. (2017). A pathology atlas of the human cancer transcriptome. Science 357, eaan2507. [PubMed: 28818916]

Consortium UniProt (2021). UniProt: the universal protein knowledgebase in 2021. Nucleic Acids Res 49 (D1), D480–D489. [PubMed: 33237286]

Wang Z, Michaud GA, Cheng Z, Zhang Y, Hinds TR, Fan E, Cong F, and Xu W (2012). Recognition of the iso-ADP-ribose moiety in poly(ADP-ribose) by WWE domains suggests a general mechanism for poly(ADP-ribosyl)ation-dependent ubiquitination. Genes Dev 26, 235–240. [PubMed: 22267412]

Wilk A, Hayat F, Cunningham R, Li J, Garavaglia S, Zamani L, Ferraris DM, Sykora P, Andrews J, Clark J, et al. (2020). Extracellular NAD^+ enhances PARP-dependent DNA repair capacity independently of CD73 activity. Sci. Rep 10, 651. [PubMed: 31959836]

Wilson DM 3rd, and Barsky D (2001). The major human abasic endonuclease: formation, consequences and repair of abasic lesions in DNA. Mutat. Res 485, 283–307. [PubMed: 11585362]

Yaku K, Okabe K, Hikosaka K, and Nakagawa T (2018). NAD Metabolism in Cancer Therapeutics. Front. Oncol 8, 622. [PubMed: 30631755]

Yang KS, Kohler RH, Landon M, Giedt R, and Weissleder R (2015). Single cell resolution in vivo imaging of DNA damage following PARP inhibition. Sci. Rep 5, 10129. [PubMed: 25984718]

Yang Y, Mohammed FS, Zhang N, and Sauve AA (2019). Dihydronicotinamide riboside is a potent NAD^+ concentration enhancer *in vitro* and *in vivo*. J. Biol. Chem 294, 9295–9307. [PubMed: 30948509]

Yang Y, Zhang N, Zhang G, and Sauve AA (2020). NRH salvage and conversion to NAD^+ requires NRH kinase activity by adenosine kinase. Nat. Metab 2, 364–379. [PubMed: 32694608]

Highlights

- Recruitment of Polβ to sites of DNA damage is dependent on XRCC1 and PAR
- Polβ mediates the dissociation of XRCC1 from sites of DNA damage
- PARP1 and PARP2 show unique DNA damage-recruitment profiles dependent on Polβ or XRCC1
- Loss of SIRT6 impairs Polβ and XRCC1 complex assembly without altering PAR formation

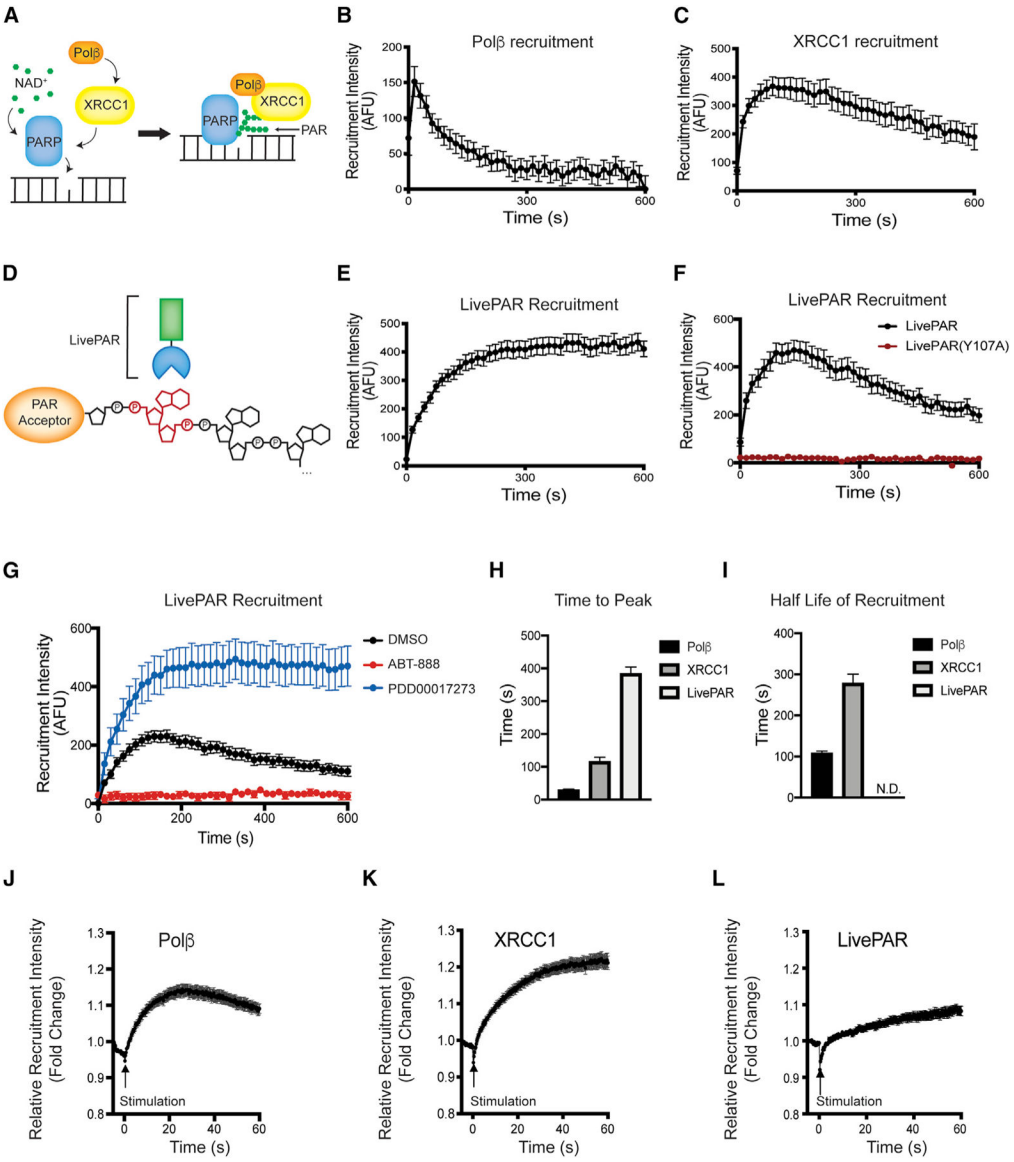

Figure 1. Laser-induced micro-irradiation: Polβ, XRCC1, and LivePAR

(A) Model for Polβ/XRCC1/PAR complex formation.

(B) Recruitment of EGFP-Polβ in U2OS cells.

(C) Recruitment of XRCC1-EGFP in U2OS cells.

(D) Model of LivePAR's mode of action. LivePAR contains EGFP fused to a poly(ADP-ribose) (PAR)-binding motif that binds to the iso-ADP-ribose moiety (shown in red).

(E) Recruitment of LivePAR in U2OS cells.

(F) Recruitment of LivePAR and LivePAR(Y107A) in A549 cells.

(G) Inhibition of PARP1/PARP2 or PARG alters LivePAR recruitment to sites of laser micro-irradiation in A549 cells.

(H) Time to peak recruitment intensity of Polβ, XRCC1, and LivePAR in U2OS cells.

(I) Half-life of recruitment of Polβ, XRCC1, and LivePAR in U2OS cells. N.D., not detected.

(J) Serial micro-irradiation of EGFP-Polβ in U2OS cells.
(K) Serial micro-irradiation of XRCC1-EGFP in U2OS cells.
(L) Serial micro-irradiation of LivePAR in U2OS cells.
For (B), (C), and (E)–(L), error bars indicate standard error of the mean, $n \geq 35$. All laser micro-irradiation was performed at 355 nm. See Figures S1–S3.

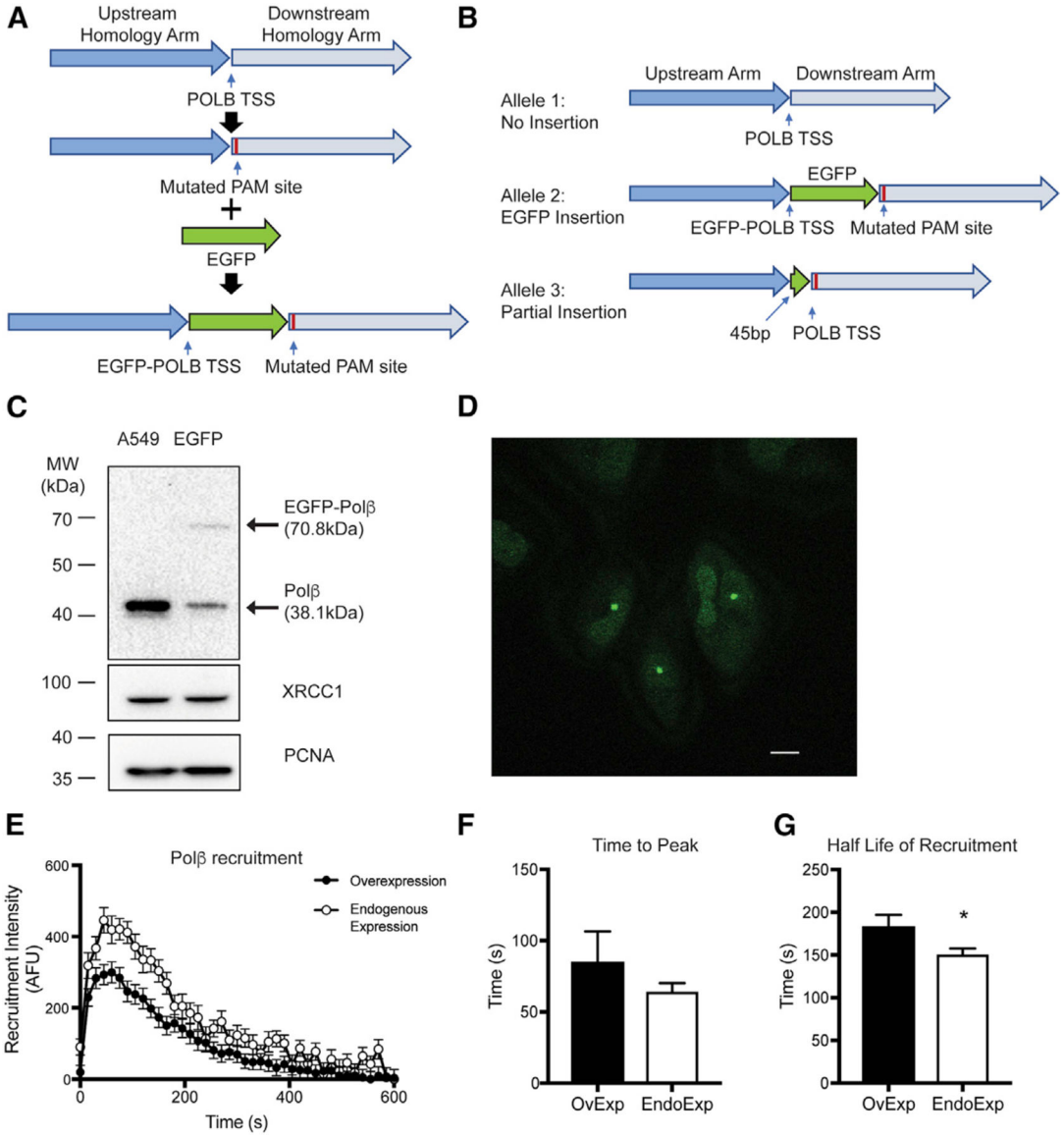

Figure 2. Overexpression of EGFP-Polβ recruits similarly to endogenously tagged EGFP-Polβ

(A) Genomic editing strategy to target the POLB gene in A549 cells. EGFP cDNA was inserted in-frame with the transcriptional start site of POLB, and a silent mutation was placed at the PAM site to prevent re-cleavage by Cas9.

(B) Allele sequencing results. Of the three alleles in A549 cells, one was not modified, one was modified with the full-length EGFP in-frame with POLB exon 1, and one allele displayed a partial 45-bp insertion. Full sequencing results are in Table S2.

(C) Immunoblot of A549 and endogenously tagged A549 cells.

(D) Spectrally unmixed image of endogenously tagged EGFP-Polβ in A549 cells. Foci in the image demonstrates EGFP-Polβ recruitment. Scale bar denotes 10 mm distance.

(E) Recruitment of endogenous EGFP-Polβ (open circles) and overexpressed EGFP-Polβ (closed circles).

(F) Time to peak recruitment intensity of endogenous EGFP-Polβ and overexpressed EGFP-Polβ following micro-irradiation. No significant difference was observed (Student's t test).
(G) Half-life of recruitment of endogenous EGFP-Polβ and overexpressed EGFP-Polβ following micro-irradiation. A significant difference ($p < 0.05$) was observed (Student's t test).
For (E)–(G), error bars indicate standard error of the mean, n R 35. All laser micro-irradiation was performed at 355 nm. See Figure S4.

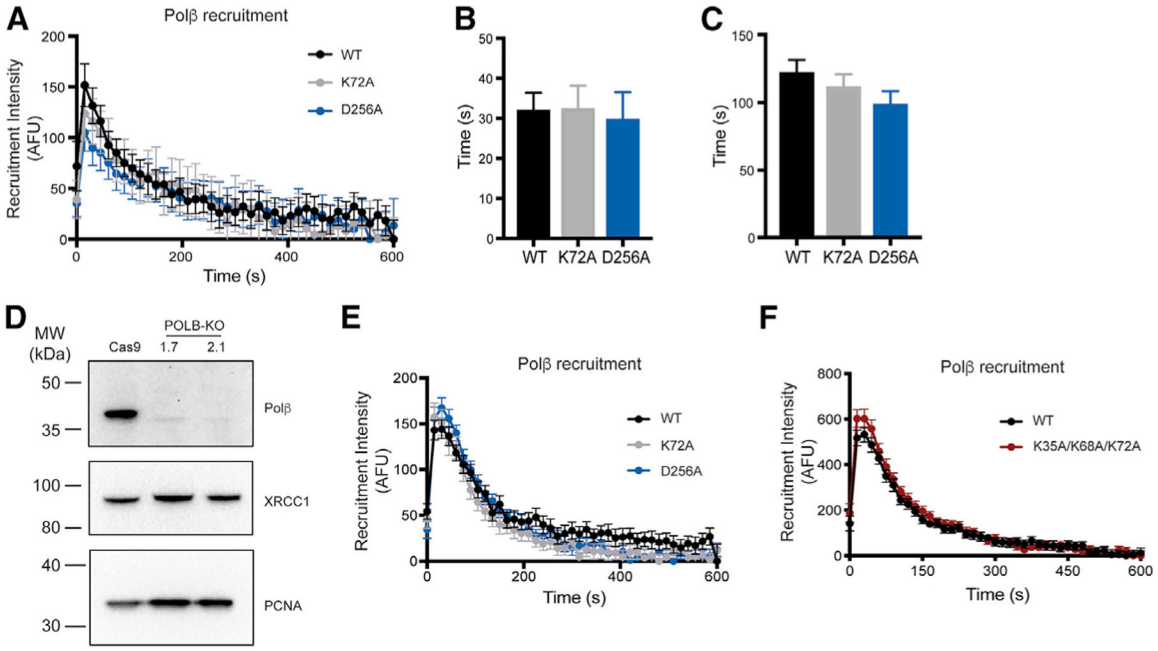

Figure 3. Loss of Polβ enzymatic activity does not alter its recruitment kinetics

(A) Recruitment of EGFP-Polβ, dRP lyase mutant EGFP-Polβ(K72A), and polymerase mutant EGFP-Polβ(D256A) in U2OS cells. Cells retained endogenous Polβ.

(B) Time to peak recruitment intensity of EGFP-Polβ, EGFP-Polβ(K72A), and EGFP-Polβ(D256A) in U2OS cells.

(C) Half-life of recruitment of EGFP-Polβ, EGFP-Polβ(K72A), and EGFP-Polβ(D256A).

(D) Immunoblots of Polβ, XRCC1, and PCNA of whole-cell protein lysates prepared from U2OS/Cas9 and two separate U2OS/POLB-KO cells, generated using two different guide RNAs.

(E) Recruitment of EGFP-Polβ, dRP lyase mutant EGFP-Polβ(K72A), and polymerase mutant EGFP-Polβ(D256A) in U2OS/POLB-KO(1.7).

(F) Recruitment of EGFP-Polβ and dRP lyase triple mutant EGFP-Polβ(K35A/K68AK72A) in U2OS/POLB-KO(1.7).

For (A)–(C), (E), and (F), error bars indicate standard error of the mean, n ≥ 35. All laser micro-irradiation was performed at 355nm. See Figure S5.

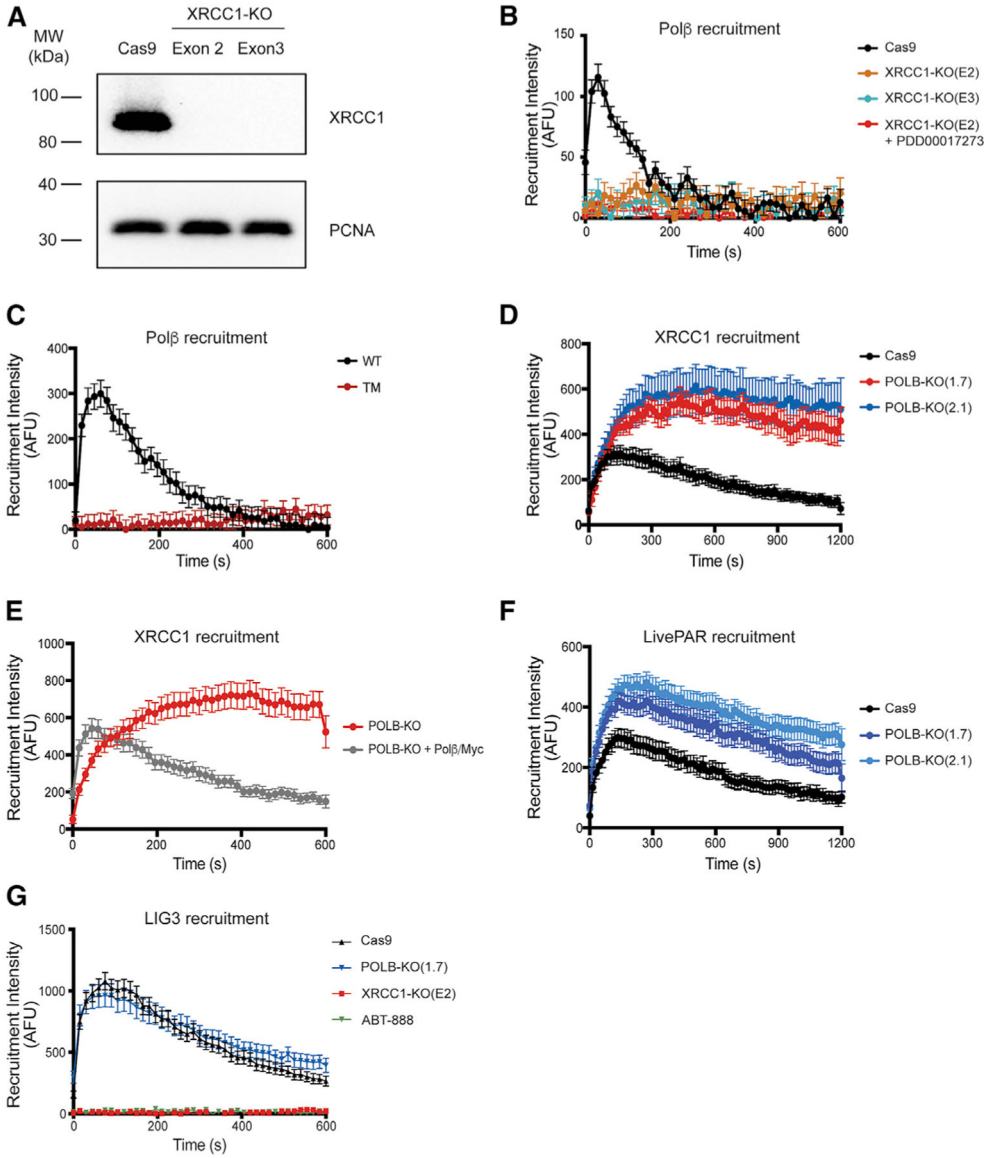

Figure 4. Recruitment of Polβ is dependent on XRCC1, while Polβ enables XRCC1 complex dissociation

(A) Immunoblots of XRCC1 and PCNA of whole-cell protein lysates prepared from U2OS/Cas9 and two separate U2OS/XRCC1-KO cells, generated using two different guide RNAs.

(B) Recruitment of EGFP-Polβ when expressed in XRCC1-KO cells with and without PARG inhibition (PDD00017273).

(C) Recruitment of EGFP-Polβ(WT) and the XRCC1-binding-deficient triple-mutant EGFP-Polβ(L301R/V303R/V306R, TM) when expressed in A549 cells.

(D) Recruitment of XRCC1-EGFP when expressed in U2OS/POLB-KO cells.

(E) Recruitment of XRCC1-EGFP when expressed in U2OS/POLB-KO cells with Polβ expression restored.

(F) Recruitment of LivePAR when expressed in U2OS/POLB-KO cells.

(G) Recruitment of EGFP-LIG3 in U2OS/Cas9, U2OS/POLB-KO(1.7), and U2OS/XRCC1-KO(E2) cells or following PARP inhibition (ABT-888).

For (B)–(G), error bars indicate standard error of the mean, n ≥ 35. All laser micro-irradiation was performed at 355 nm. See Figures S6–S8.

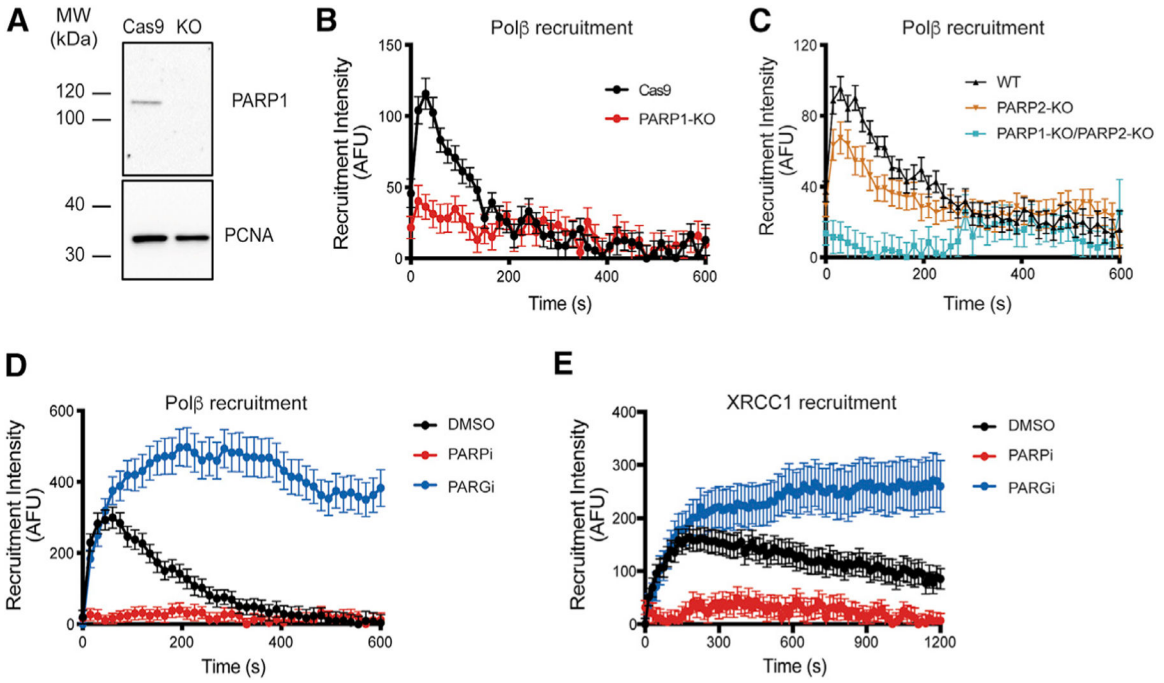

Figure 5. Polβ and XRCC1 complex dynamics are dependent on PAR

(A) Immunoblot of PARP1 in U2OS/Cas9 and U2OS/PARP1-KO cells.

(B) Recruitment of EGFP-Polβ in U2OS/PARP1-KO cells.

(C) Recruitment of EGFP-Polβ in U2OS, U2OS/PARP2-KO or U2OS/PARP1-KO/PARP2-KO cells.

(D) Recruitment of EGFP-Polβ in A549 cells following PARP or PARG inhibition.

(E) Recruitment of XRCC1-EGFP in A549 cells following PARP or PARG inhibition.

For (B)–(E), error bars indicate standard error of the mean, n ≥ 35. All laser micro-irradiation was performed at 355 nm. See Figure S9.

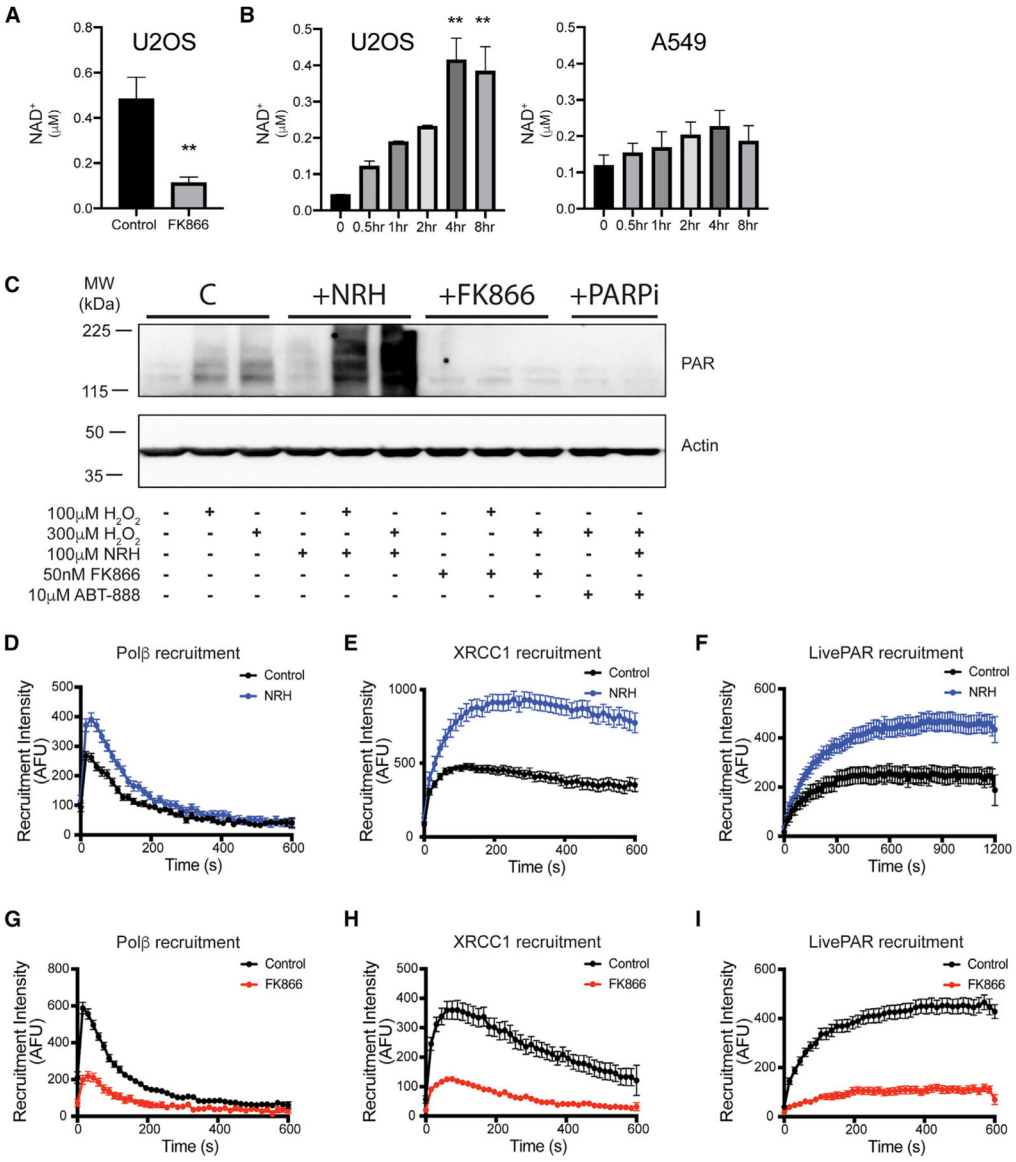

Figure 6. Polβ and XRCC1 complex dynamics are regulated by NAD$^+$ bioavailability

(A) NAD$^+$ concentrations in U2OS cells following treatment with FK866, n = 12. FK866 reduced NAD$^+$ concentrations (**p < 0.01; Student's t test).

(B) Time course of NAD$^+$ levels in U2OS cells following NRH treatment (100 μM), n = 6. NRH increased cellular NAD$^+$ concentrations in U2OS cells (**p < 0.01; one-way ANOVA, Tukey post hoc test), but not in A549 cells.

(C) Immunoblots of PAR formation in U2OS cells with H_2O_2 alone (100 μM or 300 μM, 15 min) or following pre-treatments of NRH (100 μM, 4 h), FK866 (50 nM, 24 h), or ABT-888 (10 mM, 1 h).

(D) Recruitment of EGFP-Polβ in U2OS cells following NRH treatment.

(E) Recruitment of XRCC1-EGFP in U2OS cells following NRH treatment.

(F) Recruitment of LivePAR in U2OS cells following NRH treatment.

(G) Recruitment of EGFP-Polβ in U2OS cells following FK866 treatment.

(H) Recruitment of XRCC1-EGFP in U2OS cells following FK866 treatment.
(I) Recruitment of LivePAR in U2OS cells following FK866 treatment. For (A), (C), (G)–(I), FK866 treatment was 50 nM for 24 h. For (D)–(F), NRH treatment was 100 μM for 4 h. For (A), (B), (D)–(I), error bars indicate standard error of the mean. For (D)–(I), $n \geq 35$. All laser micro-irradiation was performed at 355 nm. See Figures S10 and S11.

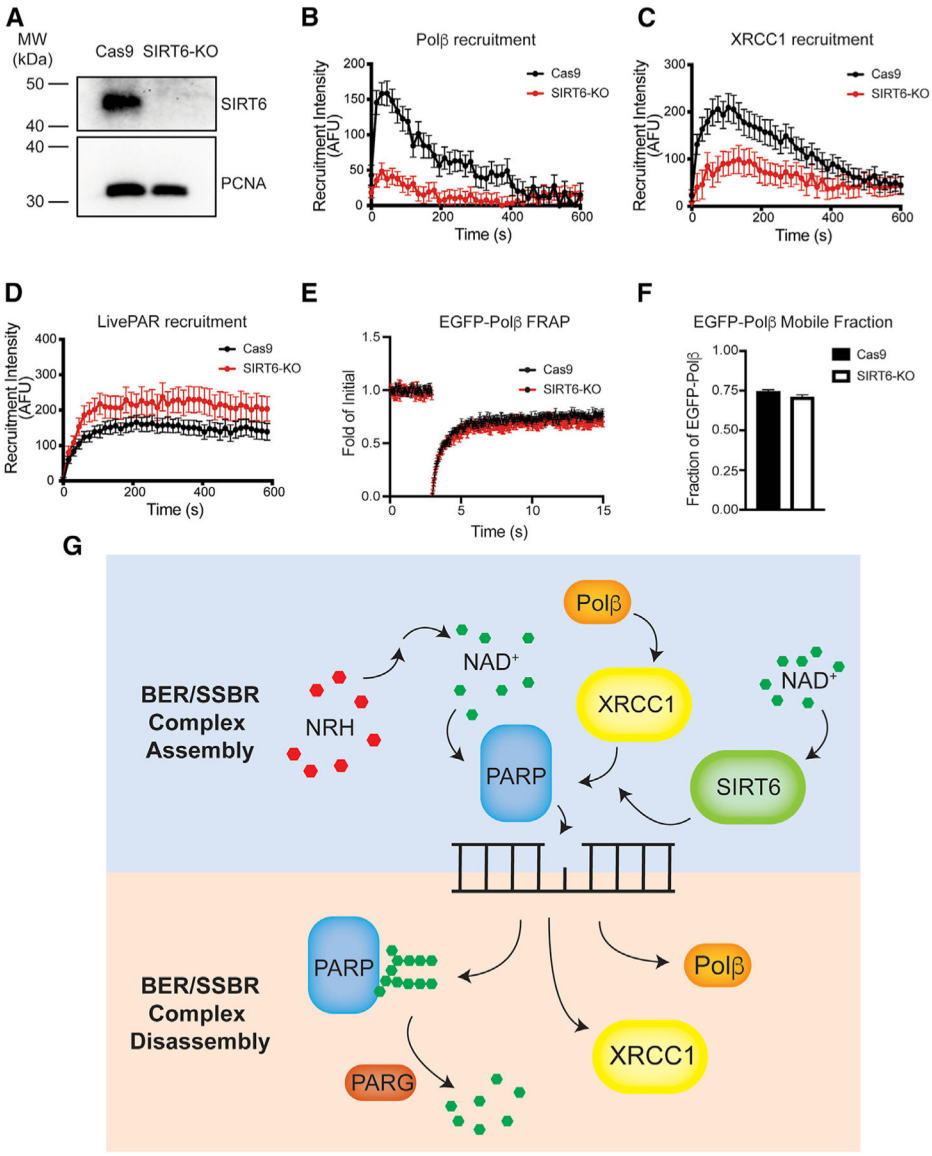

Figure 7. Loss of SIRT6 impairs Polβ and XRCC1 complex assembly, but not PAR formation

(A) Immunoblot of SIRT6 in A549/Cas9 and A549/SIRT6-KO cells.

(B) Recruitment of EGFP-Polβ in A549/Cas9 and A549/SIRT6-KO cells.

(C) Recruitment of XRCC1-EGFP in A549/Cas9 and A549/SIRT6-KO cells.

(D) Recruitment of LivePAR in A549/Cas9 and A549/SIRT6-KO cells.

(E) Fluorescence recovery after photobleaching (FRAP) traces for EGFP-Polβ in A549/Cas9 or A549/SIRT6-KO cells.

(F) FRAP-derived mobile fraction of EGFP-Polβ protein in A549/Cas9 or A549/SIRT6-KO cells. No significant difference was observed (Student's t test).

(G) Model depicting the impact of SIRT6 on PAR-dependent recruitment of XRCC1 to sites of DNA damage. PARPs initiate BER/SSBR complex assembly following micro-irradiation, with PAR formation unchanged in SIRT6-KO cells. SIRT6 regulates recruitment of XRCC1 to PAR following micro-irradiation. Reduced XRCC1 recruitment in SIRT6-KO

cells reduces the recruitment of XRCC1 binding proteins such as Polβ. BER/SSBR complex disassembly appears unaffected.

For (A)–(F), error bars indicate standard error of the mean, n ≥ 35. All laser micro-irradiation was performed at 355 nm. See Figure S12.

KEY RESOURCES TABLE

REAGENT or RESOURCE	SOURCE	IDENTIFIER
Antibodies		
Rabbit anti-XRCC1 (Immunoblot-1:2500)	Bethyl Laboratories	Cat# A300–065A
Mouse anti-Polβ (Clone 61) (Immunoblot-1:1000)	Thermo Fisher Scientific	Cat# MA5–12066
Rabbit anti-Polβ (Immunoblot-1:1000)	Abcam	Cat# ab175197
Mouse anti-PARP1 (Immunoblot-1:1000)	Santa Cruz	Cat# sc-8007
Mouse anti-PARP2 (Immunoblot-1:50)	Enzo Life Sciences	Cat# ALX-804–639-L001
Rabbit anti-C6orf130 (TARG) (Immunoblot-1:1000)	Thermo Fisher Scientific	Cat# 25249–1-AP
Rabbit anti-SIRT6 (Immunoblot-1:1000)	Novus Biologicals	Cat# NB100–2523
Mouse anti-PCNA (Immunoblot-1:2500)	Santa Cruz Biotechnology	Cat# sc-56
Mouse anti-PAR (10H) (Immunoblot-1:1000; Immunofluorescence-1:200)	Generous gift from Mathias Ziegler (University of Bergen, Norway)	N/A
Mouse anti-beta actin (Immunoblot-1:2500)	Sigma	Cat# A5441
Rabbit anti-beta actin (Immunoblot-1:1000)	Santa Cruz Biotechnology	Cat# ab8227
Rabbit anti-Myc-Tag (Immunoblot-1:1000)	Cell Signaling Technology	Cat# 2278S
Rabbit anti-gH2AX (Immunoblot-1:1000)	Trevigen	Cat# 2305-PC-100
Immun-Star Goat anti-mouse-HRP conjugate (Immunoblot-1:2500)	Bio-Rad	Cat# 170–5047
Immun-Star Goat anti-rabbit-HRP conjugate (Immunoblot-1:2500)	Bio-Rad	Cat# 170–5046
Recombinant anti-gamma H2A.X (phosphoS139), rabbit monoclonal antibody EP854(2)Y (Immunofluorescence-1:500)	Abcam	Cat# ab81299
Goat anti-mouse secondary antibody, Alexa Fluor 568 (Immunofluorescence-1:500)	Thermo Fisher Scientific	Cat# A11031
Goat anti-rabbit secondary antibody, Alex Fluor Plus 647 (Immunofluorescence-1:500)	Thermo Fisher Scientific	Cat# A32733
Bacterial and virus strains		
One Shot STBL 3 Chemically Competent *E. coli*	Thermo Fisher Scientific	Cat# C737303
Chemicals, peptides, and recombinant proteins		
Fetal bovine serum	Bio-Techne	Cat# S11150
Heat-inactivated Fetal bovine serum	Bio-Techne	Cat# S11150H
Penicillin/streptomycin	Thermo Fisher Scientific	Cat# 15140–122
DMEM	Corning	Cat# 15–017-CV
L-glutamine	Thermo Fisher Scientific	Cat# 25030–081
Dimethyl Sulfoxide	Thermo Fisher Scientific	Cat# BP231–1
Puromycin	Sigma-Aldrich	Cat# P9620–10ml
Hygromycin	Thermo Fisher Scientific	Cat# 10687010
Trypsin-EDTA	Thermo Fisher Scientific	Cat# 25200–056
0.2mM PVDF	Bio-Rad	Cat# 162–0174
0.45mM nitrocellulose	Bio-Rad	Cat# 162–0115
0.45mM Durapore Steriflip Filters	Sigma-Aldrich	Cat# SE1M003M00
Polybrene	Sigma-Aldrich	Cat# 107689

REAGENT or RESOURCE	SOURCE	IDENTIFIER
Bromodeoxyuridine (BrdU)	Sigma-Aldrich	Cat# B5002
Protease inhibitor cocktail tablets	Thermo Fisher Scientific	Cat# 88666
Blotting grade non-fat dry milk	Bio-Rad	Cat# 170–6404
Nupage 4–12% Bis-Tris gel	Invitrogen	Cat# NP0323BOX
Clarity Western ECL Substrate	Bio-Rad	Cat# 1705060
SuperSignal West Femto Maximum Sensitivity Substrate		
Thermo Fisher Scientific	Cat# 34095	
DC protein assay kit	Bio-Rad	Cat# 5000112
ABT-888 (Veliparib)	Selleckchem	Cat# S1004
PDD00017273	Sigma-Aldrich	Cat# SML1781
FK866	National Institute of Mental Health Chemical Synthesis and Drug Supply Program (Bethesda, MD).	N/A
1-[(2R,3R,4S,5R)-3,4-Dihydroxy-5-(hydroxymethyl)tetrahydrofuran-2-yl]-4H-pyridine-3-carboxamide (NRH)	Marie Migaud	Giroud-Gerbetant et al., 2019
QIAprep Spin Miniprep Kit	QIAGEN	Cat# 27106
QIAGEN DNeasy Blood and Tissue Kit	QIAGEN	Cat# 69504
Hydrogen Peroxide (9.8M)	Sigma-Aldrich	Cat# H1009
Hoechst 33342	Thermo Fisher Scientific	Cat# 62249
Formaldehyde solution (37%)	Thermo Fisher Scientific	Cat# BP531–500
Normal Goat Serum (lyophilized)	Thermo Fisher Scientific	Cat# NC9660079
NucBlue Fixed Cell Stain Ready Probes	Thermo Fisher Scientific	Cat# R37606
Alexa Fluor 647 Phalloidin	Thermo Fisher Scientific	Cat# A22287
Alt-R CRISPR S.p. Cas9 Nuclease 3NLS	IDT	Cat# 1074182
Alt-R CRISPR-Cas9 tracrRNA	IDT	Cat# 1072533
Opti-MEM I Reduced Serum Medium	Thermo Fisher Scientific	Cat# 31985062
Lipofectamine RNAiMAX Transfection Reagent	Thermo Fisher Scientific	Cat# 13778075
QuikChange II XL Site-directed Mutagenesis Kit	Agilent	Cat# 200521
TransIT-X2 Transfection Reagent	Mirus Bio	Cat# MIR 6005
EnzyChrom NAD^+/NADH assay kit	BioAssay Systems	Cat# EZND-100
FastDigest MluI	Thermo Fisher Scientific	Cat# FD0564
FastDigest BamHI	Thermo Fisher Scientific	Cat# FD0054
T7 DNA Ligase	New England Biolabs	Cat# M0318
RNase	Thermo Fisher Scientific	Cat# EN0531
Propidium Iodide	Sigma-Aldrich	Cat# P4170
Experimental models: Cell lines		
U2OS (Human osteosarcoma tumor cell line)	ATCC	Cat# HTB-96
A549 (Human adenocarcinoma tumor cell line)	ATCC	Cat# CCL-185
**Modified cell lines and media formulations can be found in* Table S4.		
Oligonucleotides		
**Complete list of oligonucleotides can be found in* Table S5.		

REAGENT or RESOURCE	SOURCE	IDENTIFIER
Recombinant DNA		
pLentiCRISPRv2 (Cas9 plus cloning site for gRNA; contains a puromycin resistance cassette)	Sanjana et al., 2014	Addgene (#52961)
pLVX-Apple-53BP1trunc-Puro (Apple fused to the N terminus of a truncated 53BP1 containing amino acids 1220–1709)	Yang et al., 2015	Addgene (#69531)
pUC19	New England Biolabs	Cat# N3041
pLV-CMV-XRCC1-mCherry-Hygro (mCherry fused to the C terminus of XRCC1 & a hygromycin resistance cassette)	Wilk et al., 2020	Addgene (#176532)
pLentiCRISPRv2-Con (Cas9 plus control gRNA; contains a puromycin resistance cassette)	Generous gift from Wim Vermeulen (Erasmus MC, NL)	Slyskova et al., 2018
pLENTI-CRISPR-V2-POLB-KO-g2 (Cas9 plus POLB gRNA #2; contains a puromycin resistance cassette)	Generous gift from Wim Vermeulen (Erasmus MC, NL)	Slyskova et al., 2018
pLENTI-CRISPR-V2-XRCC1-KO-g1 (Cas9 plus XRCC1 gRNA #1; contains a puromycin resistance cassette)	Generous gift from Wim Vermeulen (Erasmus MC, NL)	Slyskova et al., 2018
pLENTI-CRISPR-V2-XRCC1-KO-g2 (Cas9 plus XRCC1 gRNA #2; contains a puromycin resistance cassette)	Generous gift from Wim Vermeulen (Erasmus MC, NL)	Slyskova et al., 2018
pLENTI-CRISPR-V2-PARP1-KO-g1 (Cas9 plus PARP1 gRNA #1; contains a puromycin resistance cassette)	Generous gift from Wim Vermeulen (Erasmus MC, NL)	Slyskova et al., 2018
pLV-CMV-EGFP-PolB-Hygro (EGFP fused to the N terminus of Polβ &a hygromycin resistance cassette)	This study	Addgene (#176056)
pLV-CMV-XRCC1-EGFP-Hygro (EGFP fused to the C terminus of XRCC1 & a hygromycin resistance cassette)	This study	Addgene (#176062)
pLV-EF1A-LivePAR-Hygro (PAR binding domain with EGFP tag & a hygromycin resistance cassette)	This study	Addgene (#176063)
pUC19-POLBHR-eGFP (Homology region ± 800bp to the transcription start site of POLB, with EGFP inserted in-frame on the N terminus of POLB, and a mutation in the PAM site used by POLBKO gRNA1 in POLB exon1)	This study	Addgene (#176064)
pLV-Hygro-EF1A-LivePARBackbone (Expression vector with a BamHI site in frame with a Gly-Ser linker fused to EGFP; serves as the backbone for PAR binding domain incorporation for LivePAR)	This study	Addgene (#176526)
pLV-Hygro-EF1A-FHA-Linker-eGFP (EGFP fused to the C terminus of a FHA domain & a hygromycin resistance cassette)	This study	Addgene (#176065)
pLV-Hygro-EF1A-KR-Linker-eGFP (EGFP fused to the C terminus of a KR domain & a hygromycin resistance cassette)	This study	Addgene (#176066)
pLV-Hygro-EF1A-Macro-Linker- eGFP (EGFP fused to the C terminus of a Macrodomain & a hygromycin resistance cassette)	This study	Addgene (#176067)
pLV-Hygro-EF1A-OB-Linker-eGFP (EGFP fused to the C terminus of an OB domain & a hygromycin resistance cassette)	This study	Addgene (#176068)
pLV-Hygro-EF1A-PBM-Linker-eGFP (EGFP fused to the C terminus of a PBM domain & a hygromycin resistance cassette)	This study	Addgene (#176069)
pLV-Hygro-EF1A-PBZC-Linker-eGFP (EGFP fused to the C terminus of an PBZ domain & a hygromycin resistance cassette)	This study	Addgene (#176070)
pLV-Hygro-EF1A-RG-Linker-eGFP (EGFP fused to the C terminus of an RG domain & a hygromycin resistance cassette)	This study	Addgene (#176071)
pLV-Hygro-EF1A-WWE-Linker-eGFP (EGFP fused to the C terminus of a WWE domain & a hygromycin resistance cassette)	This study	Addgene (#176072)
pLV-EF1A-LivePAR(Y107A)-Hygro (EGFP fused to the C terminus of a WWE domain containing a point mutation to convert Tyr107 to Ala & a hygromycin resistance cassette)	This study	Addgene (#176073)
pLV-Hygro-EF1A-BRCT1-Linker-eGFP (EGFP fused to the C terminus of a BRCT1 domain & a hygromycin resistance cassette)	This study	Addgene (#176074)
pLV-Hygro-EF1A-XL1/BRCT1-Linker-eGFP (EGFP fused to the C terminus of a XL1/BRCT1 domain & a hygromycin resistance cassette)	This study	Addgene (#176084)

REAGENT or RESOURCE	SOURCE	IDENTIFIER
pLV-Hygro-EF1A-XL1/BRCT2-Linker-eGFP (EGFP fused to the C terminus of a BRCT2 domain & a hygromycin resistance cassette)	This study	Addgene (#176085)
pLV-CMV-EGFP-PolB-PAMmut-Hygro (EGFP fused to the N terminus of POLB containing a mutation in the PAM site used by POLBKOg1 & a hygromycin resistance cassette)	This study	Addgene (#176086)
pLV-CMV-EGFP-PolB(K72A)-PAMmut-Hygro (EGFP fused to the N terminus of POLB containing mutation in Lys72, a mutation in the PAM site used by POLBKOg1 & a hygromycin resistance cassette)	This study	Addgene (#176087)
pLV-CMV-EGFP-PolB(D256A)-PAMmut-Hygro-(EGFP fused to the N terminus of POLB containing mutation in Asp256, a mutation in the PAM site used by POLBKOg1 & a hygromycin resistance cassette)	This study	Addgene (#176088)
pLV-EGFP-PolB(K35A/K68A/K72A)-PAMmut-Hygro- (EGFP fused to the N terminus of POLB containing mutations Lys35Ala, Lys68Ala, Lys72Ala, a mutation in the PAM site used by POLB gRNA1 & a hygromycin resistance cassette)	This study	Addgene (#176089)
pLentiCRISPRv2-POLB-KO-g1 (Cas9 plus POLB gRNA #1; contains a puromycin resistance cassette)	This study	Addgene (#176090)
pLV-Hygro-EF1a-XRCC1-EGFP-T2A-myc-POLB(PAMmut) (EGFP fused to the C terminus of XRCC1, linked by T2A to N terminus MYC-tagged POLB with a mutation in the PAM site used by POLBKO gRNA1 & a hygromycin resistance cassette)	This study	Addgene (#176139)
pLV-Hygro-EF1a-XRCC1-EGFP-T2A-myc-POLB(K35A/K68A/K72/PAMmut) (EGFP fused to the C terminus of XRCC1, linked by T2A to N terminus MYC-tagged POLB with mutations Lys35Ala, Lys68Ala, Lys72Ala, and a mutation in the PAM site used by POLBKO gRNA1 & a hygromycin resistance cassette)	This study	Addgene (#176140)
pLV-Hygro-EF1a-XRCC1-EGFP-T2A-myc-POLB(D256A/PAMmut) (EGFP fused to the C terminus of XRCC1, linked by T2A to N terminus MYC-tagged POLB with a mutation in Asp256Ala, a mutation in the PAM site used by POLBKO gRNA1 & a hygromycin resistance cassette)	This study	Addgene (#176141)
pLV-Hygro-EF1a-EGFP-PolB-T2A-myc-SIRT6(PAMmut) (EGFP fused to the N terminus of POLB, linked by T2A to N terminus of SIRT6 with a mutation in the PAM site used by SIRT6-KO gRNA1 & a hygromycin resistance cassette)	This study	Addgene (#176142)
pLV-Hygro-EF1a-EGFP-PolB-T2A-myc-SIRT6(PAMmut-R65A) (EGFP fused to the N terminus of POLB, linked by T2A to N terminus of SIRT6 with a mutation in Arg65Ala, a mutation in the PAM site used by SIRT6-KO gRNA1 & a hygromycin resistance cassette)	This study	Addgene (#176143)
pLV-Hygro-EF1a-EGFP-PolB-T2A-myc-SIRT6(PAMmut-G60A) (EGFP fused to the N terminus of POLB, linked by T2A to N terminus of SIRT6 with a mutation in Gly60Ala, a mutation in the PAM site used by SIRT6-KO gRNA1 & a hygromycin resistance cassette)	This study	Addgene (#176144)
pLV-Hygro-EF1a-EGFP-PolB-T2A-myc-SIRT6(PAMmut-S56A) (EGFP fused to the N terminus of POLB, linked by T2A to N terminus of SIRT6 with a mutation in Ser56Ala, a mutation in the PAM site used by SIRT6-KO gRNA1 & a hygromycin resistance cassette)	This study	Addgene (#176145)
pLV-Hygro-EF1A-EGFP-PARP1 (EGFP fused to the N terminus of PARP1 & a hygromycin resistance cassette)	This study	Addgene (#176146)
pLV-Hygro-EF1A-PARP2-EGFP (EGFP fused to the C terminus of PARP2 & a hygromycin resistance cassette)	This study	Addgene (#176147)
pLV-Hygro-EF1A-EGFP-LIG3 (EGFP fused to the N terminus of LIG3 & a hygromycin resistance cassette)	This study	Addgene (#176148)
pLVX-CMV-XRCC1-gRNA res-Neo (XRCC1 with dual PAM resistance to XRCC1 gRNA1 and XRCC1 gRNA2 & a neomycin/G418 resistance cassette)	This study	Addgene (#176149)
pLV-Hygro-EF1A-myc-POLB(PAMmut) (Myc fused to the N terminus of POLB containing a mutation in the PAM site used by POLB gRNA1 & a hygromycin resistance cassette)	This study	Addgene (#176150)

Software and algorithms

REAGENT or RESOURCE	SOURCE	IDENTIFIER
ImageJ	ImageJ	https://imagej.nih.gov/ij/ Versions 1.48v-1.53j
FIJI	(Schindelin et al., 2012)	https://fiji.sc/
Adobe Illustrator (for preparation of figures)	Adobe Systems	https://www.adobe.com/products/illustrator.html Version 2021
GraphPad Prism	GraphPad	https://www.graphpad.com/ Version 8 (Mac OS X)
MIDAS	This manuscript	https://zenodo.org/record/5534950
NIS-Elements	Nikon Instruments	https://www.microscope.healthcare.nikon.com/en_EU/products/software/nis-elements Versions 4.51 and 5.11
Modfit LT Software (for flow cytometry)	Verity Software House	http://www.vsh.com/products/mflt/ Version 4.1